RSC Advances

REVIEW

View Article Online
View Journal | View Issue

Surface engineering and functionalization of powder-based materials by fluidized-bed atomic layer deposition for emerging applications

Hao Van Bui, *[a] Viet Phuong Cao, [a] Daoyin Liu,[b] J. Ruud van Ommen [c] and Se-Hun Kwon [d]

The growing need for advanced materials with tunable properties has triggered an increasing interest in innovative surface modification techniques. Fluidized-bed atomic layer deposition (FB-ALD) offers a powerful solution for surface engineering and functionalization of powder-based materials for a variety of applications. By relying on its capability for controlling uniformity and conformality of the coatings precisely at the atomic scale, ALD can effectively modify surface characteristics to improve the functionality and durability of the materials. In this review, we will provide comprehensive fundamentals and strategies to improve the fluidization of nanopowders and reveal the potential of FR-ALD in two emerging applications. The first application is in energy devices, where FB-ALD is employed to develop Pt-based electrocatalysts for fuel cells and other catalytic reactions. We demonstrate that FB-ALD enables precise control of size, composition, and dispersion of Pt nanoparticles over the support surface, resulting in a strong enhancement in catalytic performance. We additionally discuss the application of FB-ALD in boosting the stability and durability of catalysts by surface engineering with ultrathin films and ultrasmall nanoparticles without compromising their activity. These capabilities open new avenues for the development of high-performance and durable catalysts for energy applications. The second application is in pharmaceutical research, where FB-ALD is employed to coat active pharmaceutical

[a]Faculty of Materials Science and Engineering, Phenikaa University, Hanoi 12116, Vietnam. E-mail: hao.buivan@phenikaa-uni.edu.vn
[b]School of Energy and Environment, Southeast University, Nanjing 210096, China
[c]Department of Chemical Engineering, Delft University of Technology, Van der Maasweg 9, Delft 2629 HZ, The Netherlands
[d]School of Materials Science and Engineering, Pusan National University, 30 Jangjeon-Dong Geumjeong-Gu, Busan 46241, Republic of Korea

Hao Van Bui

Hao Van Bui is an associate professor and currently serves as vice director of the Phenikaa Institute for Advanced Study, Phenikaa University, Vietnam. He received his MSc degree in Materials Science from Hanoi University of Science and Technology, in 2008, and his PhD degree in Electrical Engineering from the University of Twente, the Netherlands, in 2013. He was a postdoctoral researcher at the University of Twente and Delft University of Technology (2013–2017). Since November 2018, he has been leading the ALD Research Group at Phenikaa University. His research focuses on ALD for applications in energy, catalysis, pharmaceuticals, and semiconductor technologies.

Viet Phuong Cao

Viet Phuong Cao received his BSc degree in Pharmacy from Hanoi University of Pharmacy, Vietnam, in 2019, and subsequently obtained his MSc degree in Pharmaceutical Sciences from Seoul National University, South Korea, in 2023. He joined the ALD Research Group at Phenikaa University as a researcher in April 2023, where his work focuses on the application of atomic layer deposition (ALD) and molecular layer deposition (MLD) to modify the properties of active pharmaceutical ingredients (APIs).

ingredients with thin films of biocompatible materials, such as Al_2O_3, ZnO, SiO_2, and TiO_2, to control their release profiles and improve their physical properties, such as wettability, dispersibility, flowability, and solubility, which are essential for enhancing therapeutic efficacy and patient compliance. The versatility and precision of FB-ALD position it as a key technology for the development of next-generation materials, addressing the critical challenges of performance, stability, and functionality of powder-based materials for different fields.

Introduction

Powder-based materials are fundamental to a wide range of industrial and technological applications, including catalysis and energy, environmental and sustainable technologies, advanced ceramics and composites, aerospace and automotive, metallurgy and refractory, additive manufacturing, pharmaceuticals and healthcare. Their high surface area and tunable properties make them essential for optimizing performance in these fields. Because powder-based materials consist of finely divided particles with high specific surface areas, they exhibit enhanced interactions with their surrounding environments., which is particularly valuable in applications requiring high surface-to-volume ratios. For instance, in catalysis, the high surface area of these materials can provide more accessible reaction sites, which may improve reaction efficiency under certain conditions. Similarly, in energy storage systems, such as batteries and supercapacitors, powder-based materials serve as key components in electrode fabrication, acting as catalysts to enhance electrochemical reactions and improve charge storage capacity. Despite numerous advantages, powder-based materials often face challenges such as stability issues, poor dispersion, and surface degradation. These limitations may compromise their performance, particularly in harsh operational conditions where exposure to moisture, extreme temperatures, or reactive chemicals can lead to undesirable changes in material properties. To overcome these challenges, precise surface engineering techniques are required to enhance their durability, functionality, and efficiency. Surface modifications can improve particle dispersion, reduce agglomeration, and introduce specific functionalities that tailor these materials for specialized applications.

Various techniques have been developed for modifying the surface of powder-based materials, including wet-chemistry methods (*e.g.*, sol–gel, precipitation, and impregnation), physical vapor deposition (PVD), and chemical vapor deposition (CVD).[1,2] Due to their simplicity, versatility, and cost effectiveness, these techniques are widely used. However, they often face challenges in achieving uniform and conformal coatings (*i.e.*, coatings with a constant thickness over the entire substrate

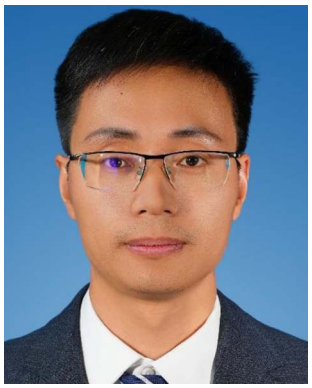

Daoyin Liu

Daoyin Liu is a full professor at the School of Energy and Environment, Southeast University, China. He obtained his PhD in Mechanical Engineering at Southeast University, China in 2011. He was a visiting researcher at Delft University of Technology, the Netherlands (2014–2015). His research areas include fluidization, multiphase reactor simulation, and particle coating.

J. Ruud van Ommen

J. Ruud van Ommen is a full professor in the Chemical Engineering department, Delft University of Technology, the Netherlands. His group focuses on multiphase reactor engineering, particle technology, and scalable production of nanostructured materials. He is a member of the management teams of the e-Refinery Institute and the Process and Product Technology Institute (Pro2Tech). He obtained his MSc degree in Chemical Engineering at Delft University of Technology in 1996, and in 2001 a PhD degree at the same university. He has been a visiting professor at Chalmers University (Gothenburg, Sweden) and the University of Colorado (Boulder, USA). He is co-founder of Delft IMP (now called Powall), a spin-off company from his group.

Se-Hun Kwon

Se-Hun Kwon is a full professor at Pusan National University, South Korea. He obtained his PhD from KAIST, South Korea, in 2008. He is currently the director of the Institute of Materials Technology and the director of the BK21FOUR Program (Innovative Graduate Education Program for Global High-Tech Materials and Parts, School of Materials Science and Engineering, Pusan National University). His research focuses on ALD for fabricating smart functional nanomaterials, interface materials, and highly ordered nanostructures, with applications in semiconductors, fuel cells, photoelectrochemical systems, nanopatterning, and advanced hard coatings.

surface) on complex, high-surface-area powders. For instance, wet-chemistry approaches can suffer from limited control over film thickness, PVD methods typically provide line-of-sight deposition that is unsuitable for deep or tortuous surfaces, while conventional CVD may lead to non-uniform film growth on cohesive or poorly fluidized powders. One of the most advanced techniques for modifying the surface of powder-based materials is atomic layer deposition (ALD).[1,3–7] This is a vapor-phase technique that enables the controlled deposition of thin films or nanoparticles (NPs) of various materials, including metals, oxides, nitrides and many other compounds, with atomic precision and unprecedented uniformity.[8] In ALD, the substrate surface is alternately and sequentially exposed to reactive gaseous precursors in cycles.[9–11] A typical ALD cycle consists of four key steps: precursor A exposure, purge, precursor B exposure, and purge (Fig. 1a). Each precursor reacts only with specific surface functional groups and, once all the available reactive sites are consumed, the reaction reaches a saturation. This self-limiting behavior ensures that each ALD cycle deposits no more than a single atomic layer of material. Repeating this cycle enables the material growth in a layer-by-layer manner, providing a precise control of material deposition at the atomic level and providing exceptional uniformity even on substrates with complex topologies or high surface areas, such as nanoparticles, high-aspect-ratio nanostructures, and porous nanostructures (Fig. 1b–d).[12–14] These capabilities make ALD a versatile tool for improving the stability, reactivity, and overall performance of powder-based materials. In catalysis, ALD is used to deposit ultra-thin films or NPs of catalytic materials, which allows for optimizing their spatial distribution and accessibility.[15–19] Additionally, ALD coatings act as protective layers that mitigate sintering, which commonly occurs when NPs tend to coalesce at high temperatures, thereby preserving catalytic activity and prolonging the operational lifespan of the catalysts.[20,21] In energy storage applications such as Li-ion and solid-state batteries, ALD-modified materials benefit from precisely engineered interfaces that mitigate electrode degradation and lithium dendrite formation, enhance ionic conductivity, and improve structural stability. By depositing conformal films, ALD enhances electrode stability by preventing undesirable side reactions, minimizing structural degradation, and stabilizing solid-electrolyte interphases.[3,22] Similarly, in fuel cells, ALD is used to deposit noble metal NPs (*e.g.*, Pt NPs) onto high-specific-area supports such as nanocarbon.[23–25] This approach ensures precise control over NP size, dispersion, and loading, maximizing catalyst utilization. Most recently, ALD has shown great potential in the pharmaceutical industry, where ALD coating enables precise control over drug particle surface properties, enhancing bioavailability, stability, and targeted delivery. By applying nanometer-thin layers of biocompatible materials such as Al_2O_3, SiO_2, and ZnO, ALD can modulate drug dissolution rates, protect sensitive active pharmaceutical ingredients from environmental degradation, and facilitate the dispersion of hydrophobic drugs in aqueous solutions, thereby improving therapeutic efficacy and patient compliance.

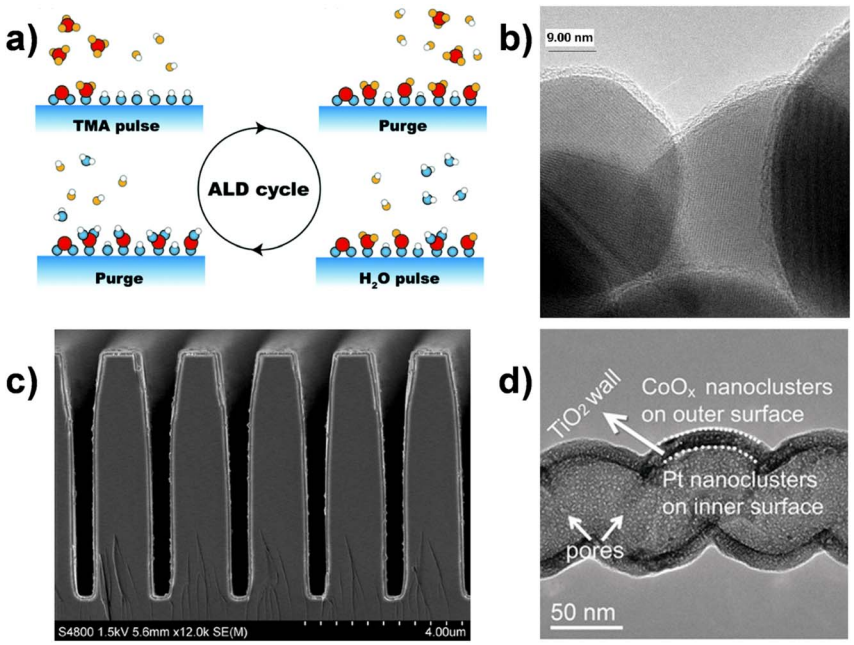

Fig. 1 (a) Schematic animation of Al_2O_3 ALD using trimethylaluminum (TMA) and H_2O including four A/B/A/B steps: exposure to TMA, purge, exposure to H_2O, and purge. Adapted from ref. 8 with permission from Royal Society of Chemistry, copyright 2017; (b) uniformity of ALD thin film on high-surface-area substrate: TEM image of ZrO_2 particles coated by BN films with a thickness of ~25 Å after 26 AB cycles at 500 K. Adapted from ref. 14 with permission from Elservier, copyright 2002; (c) SEM cross-sectional image of conformal $Ge_2Sb_2Te_5$ ALD film in trenches. Adapted from ref. 12 with permission from American Chemical Society, copyright 2009; (d) uniformity of ALD nanoparticles deposited on porous substrate: TEM images of the CoO_x and Pt NPs deposited on outer and inner walls of TiO_2 nanotubes containing micropores. Adapted from ref. 13 with permission from Wiley, copyright 2017.

Several reactor configurations have been developed for performing ALD on powder-based materials,[26,27] including fixed bed reactors,[26,28] viscous flow reactors (Fig. 2a),[29] fluidized bed reactors (FBRs, Fig. 2b),[30,31] rotary reactors (Fig. 2c),[32–34] and spatial ALD systems adapted for particulate materials (Fig. 2d).[35] Each configuration offers specific advantages but also faces limitations in terms of precursor distribution, powder mixing efficiency, and scalability, as discussed in detail in previous review articles.[4,26,27] Among these ALD reactor types for powder engineering, FBRs offer distinct advantages due to their ability to achieve uniform precursor distribution and precursor usage efficiency, and excellent powder agitation.[36–39] In an FBR, powder particles are fluidized and suspended in a stream of carrier gas, allowing for continuous motion and uniform exposure to ALD precursors. This dynamic environment ensures that the particles can achieve uniform coating. Additionally, the enhanced gas–solid interaction in FBRs facilitates efficient precursor utilization, reducing material waste and improving process scalability.[39] Furthermore, FBRs allow for feasible tuning the deposition conditions, such as temperature and pressure, in a broad range. This flexibility enables ALD processing of thermally sensitive substrates and diverse powder compositions under application-specific conditions. For instance, low-temperature and atmospheric-pressure are crucial for coating polymeric supports and pharmaceutical powders without inducing thermal degradation or phase transformation. Moreover, precise control over temperature and pressure allows for optimization of surface reaction pathways, as well as precursor adsorption and desorption behaviors, which directly influence the growth-per-cycle, the coating conformality, and the resulting material properties. These advantages make FBRs ideal for large-scale ALD applications, including catalyst synthesis, battery material modification, and pharmaceutical coatings, where high-throughput and conformal coating of fine powders are critical.

Several reviews have summarized recent advances in the application of ALD for surface modification of powder materials. For instance, Hu *et al.* focused on the reactor designs for powder ALD and their applications in various areas, such as stabilization of particles, catalysts, energetic materials, batteries, wave absorbing materials, and medicine.[1] Lee *et al.* provided a comprehensive overview of powder ALD strategies specifically for rechargeable battery materials, emphasizing the performance enhancement *via* the nanoscale coatings of electrode powders.[3] More recently, Yan *et al.* reviewed particle ALD with a primary focus on the reactor designs, followed by the discussions of representative applications in energy, catalysis, biomedicine, and cosmetics.[26] This review article focuses on surface engineering and functionalization of powder-based materials using FB-ALD. Here, the surface engineering refers to modifying the surface morphology of the powders, *i.e.*, through thin film coatings or NP deposition, while the surface functionalization focuses on tailoring the surface chemistry to impart specific functionalities, such as catalytic activity and durability of catalysts, and hydrophilicity, biocompatibility, or controlled release of pharmaceuticals. We discuss how FB-ALD enables both aspects through atomic-scale modification of the powder surfaces, emphasizing their utility in the synthesis of

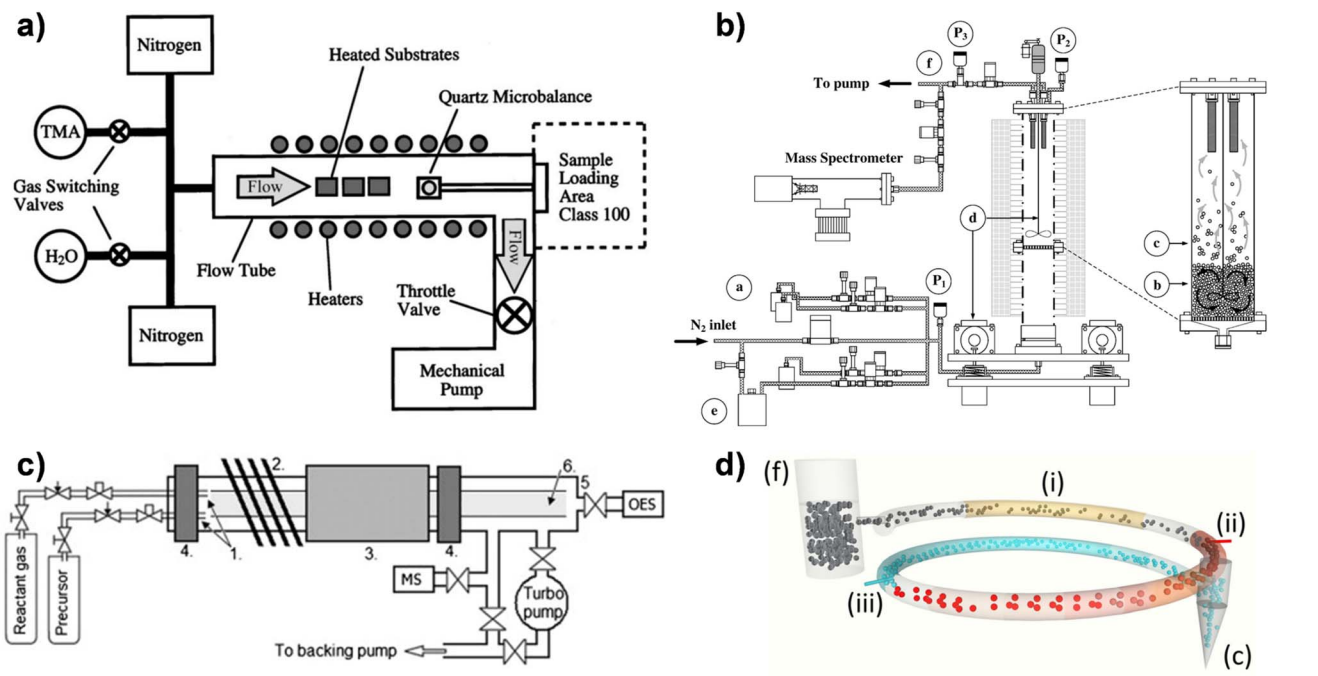

Fig. 2 Schematic diagrams of the typical ALD reactor types for powder-based materials: (a) viscous flow reactor. Adapted from ref. 29 with permission from AIP Publishing, copyright 2002; (b) fluidized bed reactor. Adapted from ref. 30 with permission from Elsevier, copyright 2007; (c) rotary reactor. Adapted from ref. 33 with permission from Elsevier, copyright 2012; (d) spatial reactor. Adapted from ref. 35 with permission from AIP Publishing, copyright 2015.

advanced Pt-based electrocatalysts and in pharmaceutical research, which represent two well-established and rapidly growing areas where FB-ALD has demonstrated clear and distinctive advantages. Pt-based electrocatalysts provide a model system for illustrating how FB-ALD allows precise control over nanoparticle size, dispersion, and stability, which are the key parameters for energy applications. In contrast, pharmaceutical powders demonstrate the versatility of FB-ALD in modifying interfacial properties and drug-release behavior in a non-catalytic context. These two application domains effectively showcase the broad utility and adaptability of FB-ALD across fundamentally different material challenges. Before delving into these applications, we provide a fundamental discussion on the fluidization of nanopowders, the challenges associated with their fluidization, and strategies to address these issues. Understanding these principles is essential for optimizing ALD processes in FBRs, ensuring uniform surface modification and improved material performance.

Fluidization of nanopowders

During fluidization, nanoparticles readily form micron-sized agglomerates due to dominant interparticle forces, including van der Waals interactions, hydrogen bonding, and electrostatic forces.[40] The conventional Geldart classification,[41] proposed for millimeter- and micrometer-sized particles, cannot be used to describe the fluidization behavior of nanoparticles. Thus, the concept of "agglomerate fluidization" has been proposed, defining nanoparticle fluidization as a process where agglomerates act as the basic fluidized elements,[42,43] The density of nanoparticle agglomerates follows a power-law relationship with size (Fig. 3), typically characterized by their fractal dimension (D_f),[44] which is a quantitative description of the complexity of the agglomerate shape. De Martín *et al.* determined that complex agglomerates (40–400 μm) exhibit a fractal dimension of 2.0–2.3 by using sedimentation or settling tube experiments and image analysis.[45] In a broad view, the reported values of D_f vary widely (1.9–2.7), depending on particle properties and fluidization conditions.[46] For instance, SiO_2 agglomerates show $D_f \approx 2.3$,[47] while TiO_2 agglomerates, usually owing to stronger surface forces, can reach $D_f \approx 2.6$.[48]

Agglomerates of nanoparticles exhibit hierarchical structures. de Martín *et al.*[44] combined spin-echo small-angle neutron scattering (SESANS) and sedimentation tube tests to characterize the three levels of structures proposed by Yao *et al.*:[49] primary aggregates (1–100 nm) with low fractal dimension ($D_{f,1} \approx 1.8$–2.1); simple agglomerates (20–100 μm) with dense packing ($D_{f,2} \approx 2.7$); complex agglomerates (100–700 μm) with looser structures ($D_{f,3} \approx 2.0$–2.3).[44] Fabre *et al.* further validated hierarchical structures, confirming different formation mechanisms for simple ($D_f \approx 2.7$) and complex agglomerates ($D_f \approx 2.2$).[50] Agglomerate stability is governed by surface forces, hydrodynamics, and fluid properties. Tahmasebpoor *et al.* demonstrated that hydrogen bonding increases interagglomerate forces by 1.3 nN in hydrophilic TiO_2, resulting in large agglomerates accounting for approximately 30% of the total agglomerate volume compared to hydrophobic TiO_2.[51] Esmailpour *et al.* observed narrowed size distributions and improved fluidization homogeneity at temperatures >200 °C, suggesting thermal suppression of agglomerate cohesion.[52]

Fluidization characteristics

The fluidization of nanoparticle agglomerates is typically divided into two regimes: agglomerate particulate fluidization (APF) and agglomerate bubbling fluidization (ABF).[53] APF behavior commonly occurs for hydrophobic nanoparticles (*e.g.*, hydrophobic SiO_2 R974) or surface-modified particles.[54] Mogre *et al.* found that adding isopropanol during the long-term fluidization of TiO_2 nanoparticles reduces electrostatic interactions, thereby promoting APF formation.[55] In ABF, Bahramian

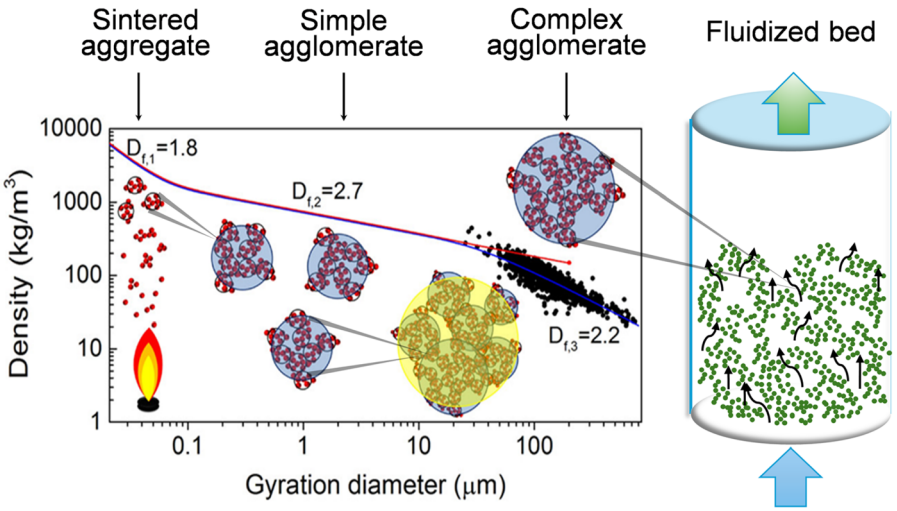

Fig. 3 Fluidized nanoparticle agglomerates are hierarchical fractal structures with three fractal dimensions: sintered aggregates formed during nanoparticle synthesis, simple agglomerates unbroken during fluidization, and large complex agglomerates broken during fluidization. Adapted from ref. 44 with permission from American Chemical Society, copyright 2014.

and Grace observed that bubble size increases with gas velocity, and the bed structure is strongly influenced by interparticle forces.[56] Gómez-Hernández *et al.* revealed through X-ray imaging and pressure signal analysis that ABF beds exhibit smooth fluidization at low gas velocities but transition to intense bubbling with pronounced hysteresis at higher velocities.[57] Additionally, ABF is prone to particle stratification, where larger agglomerates tend to settle toward the bed bottom.[55] From a processing perspective, APF is generally preferred for ALD of nanopowders, as it provides a more homogeneous bed expansion, improved gas–solid contact, and reduced particle elutriation (*i.e.*, the blowing out of particles from the bed), which are essential for achieving uniform coatings. In contrast, ABF is often associated with channeling, poor mixing, and non-uniform precursor exposure, which can lead to non-uniform precursor distribution and coating inhomogeneity.

Improving the fluidization of cohesive nanopowders

As nanopowders are dominated by strong interparticle cohesive forces that promote the agglomeration, nanopowders often exhibit poor flowability, channeling, and defluidization, leading to non-uniform gas–solid contact and limited precursor penetration. These effects can severely compromise the conformality and uniformity of ALD coatings on high-surface-area powders. Addressing these intrinsic fluidization challenges is therefore a prerequisite for the successful and scalable application of FB-ALD to nanopowder-based materials. Therefore, nanoparticle fluidization is often realized with the help of auxiliary or assistance methods. For instance, vibration strongly reduces the minimum fluidization velocity (*i.e.*, the minimum gas velocity to obtain a fluidized bed, U_{mf}) and decreases agglomerate size.[58] Vibration assistance suppresses bubbles and channels, enhancing fluidization uniformity.[59] Wu *et al.* discovered *via* X-ray imaging that comb-shaped stirrers positioned at the bed bottom effectively disrupt agglomerate structures in cohesive powders.[60] Kamphorst *et al.* demonstrated through X-ray imaging that vertical vibration eliminates channeling, but excessive vibration leads to particle compaction at the bed base.[61] Zhu *et al.* reported that a 200–600 Hz acoustic field reduces the U_{mf} of SiO_2 from 0.14 cm s^{-1} to 0.054 cm s^{-1}, with the mechanism attributed to acoustic pressure waves promoting agglomerate fragmentation.[62] Yu *et al.* utilized alternating magnetic fields to induce quasi-particulate fluidization in Fe_3O_4 nanoparticle beds.[63] Lepek *et al.* demonstrated that alternating electric fields weaken agglomerate strength by periodically altering particle charge states, reducing elutriation by 40%.[64] Ali *et al.* found that adding 5% of Geldart A particles (*i.e.*, particles typically in the 30–150 μm size range that exhibit smooth bed expansion and good gas–solid contact) triples the bed expansion ratio of nano-SiO_2.[65] Martín *et al.* reported that supercritical fluid-assisted fluidization substantially lowers the minimum fluidization velocity of TiO_2 nanoparticle agglomerates.[66] Recent studies suggest that combining multiple auxiliary methods further enhances nanoparticle agglomerate fluidization. Zhao *et al.* found that segregation of agglomerate was substantially reduced by coupling vibration with stirring (Fig. 4).[67] Zhang *et al.* designed 3D-printed hollow stirrers combined with gas jets, achieving over 50% improvement in bed expansion ratio under dual-mode assistance.[68] Combining vibration, stirring and jet methods further reduced the critical fluidization velocity and yielded more uniform agglomerate size distributions.

Modeling of fluidization

Fluidization of cohesive nanopowders involves multiscale interactions, including gas–solid hydrodynamics, interparticle forces, agglomeration and breakage dynamics.[53] Modeling approaches therefore play a critical role in rationalizing experimental observations, identifying the dominant parameters controlling fluidization regimes, and predicting system behavior under conditions that are difficult or impractical to probe experimentally.

The average agglomerate size can be predicted through force balance models. De Martín and van Ommen proposed a model incorporating van der Waals forces and hydrogen bonding, achieving theoretical predictions of agglomerate size with approximately 20% deviation from experimental results.[69] However, such average size models were not able to account for dynamic agglomerate breakage and reorganization processes. Liu *et al.* developed an adhesive computational fluid dynamics-discrete element method (CFD-DEM) model, treating simple agglomerates as discrete units and visualizing dynamic breakage and reorganization (Fig. 5a), albeit at high computational cost.[70,71] Bahramian and Olazar enhanced simulation accuracy for collision energy dissipation[71] by introducing the JKR contact model to improve cohesive force calculations.[72] Macroscopically, the dynamic evolution of agglomerate size distributions can be described using population balance models (PBM).[73] Wu *et al.* simulated the transition of nanoparticle agglomerates from fixed beds to homogeneous fluidization by using dynamic correlations between agglomeration/breakage kernel functions (Fig. 5b),[74] which is based on the critical velocity theory for agglomeration/breakage proposed by Kellogg *et al.*[75] This work revealed the regulatory mechanism of critical velocity ratios on fluidization behavior. While PBM offers computational efficiency, the universality of kernel functions still requires validation through additional experimental data.

A different modelling approach has been used by Grillo *et al.* to optimize the utilization of precursors in ALD using FBRs.[76] Rather than using CFD simulations, they developed a multiscale model combining bubbling two-phase model, precursor diffusion and reaction to study the effect of the precursor transport from the inlet of the reactor to the particles active surface and the surface reaction. Their simulations revealed that under optimal operating conditions, such as appropriate reactor height, superficial gas velocity, and pulse duration, the precursor molecules can be nearly completely consumed by surface reactions before exiting the reactor. This approach not only provides practical guidance for the rational design of FB-ALD systems but also emphasizes the importance of

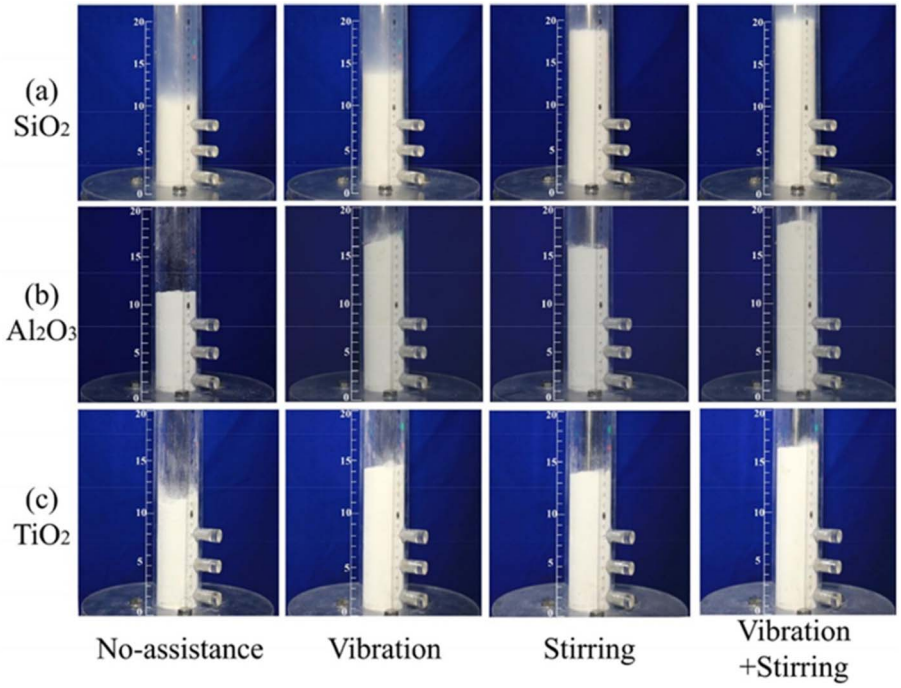

Fig. 4 Fluidization behaviors of nanoparticle agglomerates with different assisted methods. (a) SiO_2, $U_g = 0.4$ cm s^{-1}; (b) Al_2O_3, $U_g = 3.1$ cm s^{-1}; (c) TiO_2, $U_g = 5.4$ cm s^{-1}. Compared with fluidization assisted by vibration or stirring separately, the combination of the two methods can further increase the bed expansion ratio. Reproduced from ref. 67 with permission from Elsevier, copyright 2020.

balancing hydrodynamic and kinetic factors to ensure cost-effective processing.

Pt-based electrocatalysts by FB-ALD

ALD is a powerful tool for realizing next-generation catalysts for energy conversion, environmental remediation, and sustainable chemical production. It enables the deposition of a variety of materials on high-surface-area supports and provides precise control of the catalyst size, composition, and distribution at the atomic scale.[15–18] It also plays a key role in electrocatalysis and photocatalysis by engineering interfaces, tuning charge transfer properties, and enhancing durability in harsh reaction environments.[77,78] Particularly for Pt, ALD offers a unique advantage in precisely controlling NP size down to the single-atom level to maximize the catalytic performance while minimizing the

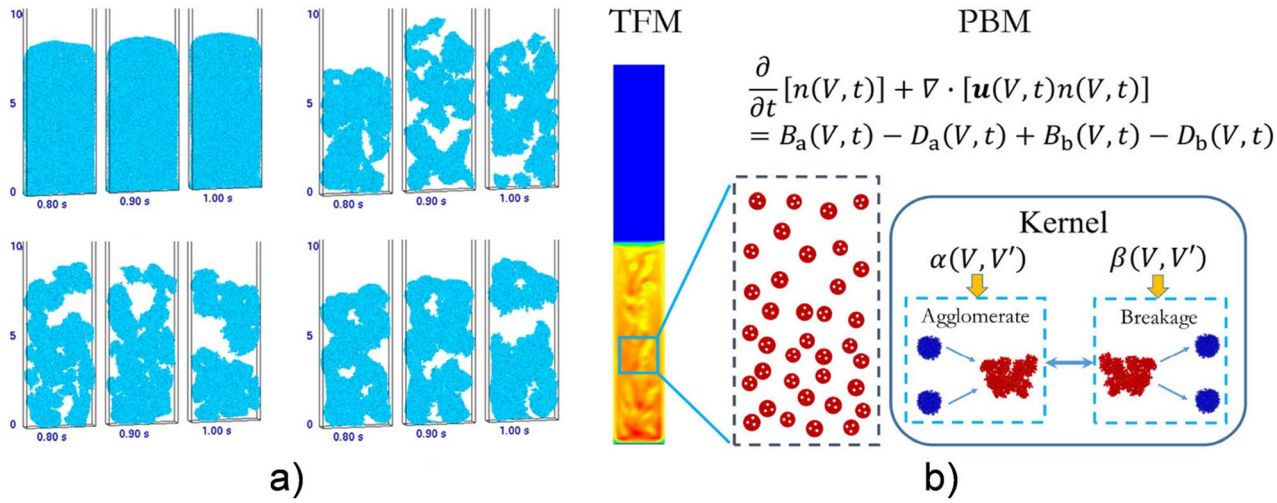

Fig. 5 (a) Snapshots of particle flow patterns simulated by adhesive CFD-DEM model under increasing cohesive force. Adapted from ref. 71 with permission from Wiley, copyright 2016. (b) Schematic of TFM-PBM model, where the TFM considers both the gas and nanoparticle agglomerates as continuums and the PBM models the number density of each class of agglomerates. Adapted from ref. 74 with permission from American Chemical Society, copyright 2024.

loading, which is crucial for scarce, expensive elements such as Pt.[79–82] In addition to monometallic Pt NPs and single-atom Pt species, ALD can also be used to synthesize more complex Pt-based nanostructures, such as core–shell[83–86] and alloy NPs.[87–89] Furthermore, ALD facilitates the catalyst surface engineering, enhancing charge transfer properties, catalytic selectivity and durability.[20,21] Importantly, by applying surface pretreatment, the nucleation and growth of Pt NPs on the supports surface can be tailored, enabling the deposition of Pt NPs with high spatial dispersion and size uniformity.[90,91] These capabilities make ALD an indispensable technique for the development of advanced Pt catalysts with enhanced performance and durability. In this part, we will discuss recent strategies to achieve controlled growth of Pt NPs on different supports by FB-ALD technology for catalytic applications.

Surface pretreatment

Surface pretreatment in ALD refers to a process of modifying the surface of substrates prior to the deposition. This is a critical step in Pt ALD as it directly influences the initial adsorption of precursor molecules and nucleation, the subsequent growth, the final uniformity, and the reproducibility of the deposition, especially on inert surfaces. Proper pretreatment adjusts the surface chemistry and creates reactive sites necessary for precursor adsorption. Several approaches, such as chemical and plasma treatments, have been utilized to enhance surface reactivity, enabling uniform deposition, especially on substrates with low wettability or high chemical inertness. For instance, Lee *et al.* demonstrated that the pretreatment of Si/SiO_2 substrates with piranha solution (*i.e.*, a mixture of concentrated sulfuric acid with hydrogen peroxide in a certain ratio) can create hydroxyl groups and increase their hydrophilicity.[92] This facilitates the adsorption precursor molecules and subsequently improves the nucleation of Pt in thermal ALD using $MeCpPtMe_3$. The inert properties of carbon cloth, which is widely used as a conductive and porous support as well as a current collector in electrocatalyst electrodes, can be altered by applying a treatment using HNO_3 vapor at 140 °C, which produced various functional groups, such as O–H, C=O and C–O, and enabled the deposition of Pt NPs.[24] The pretreatment by some other small-molecule chemicals, such as trimethylaluminum (TMA)[93–95] and NH_3,[96] has been demonstrated to enhance the nucleation of Pt. Likewise, the pretreatment in TMA or O_2 plasma, which generates surface defects or creates surface active oxygen-containing species, is another effective approach to diminishing the nucleation delay in Pt ALD.[97]

Specifically, for ALD of Pt NPs on nanocarbon powders, such as carbon black and graphene nanoplatelets, both wet and dry pretreatments have been applied. Vulcan carbon black is one of the most popular supports for Pt-based catalysts in fuel cells.[98] A pretreatment of the powder in citric acid solution at room temperature can create oxygen-containing functional groups, such as C–O and C=O, and abundant defects the carbon surface, whose densities can be controlled by the pretreatment time.[99–102] As an example for an optimal pretreatment process reported by Lee *et al.*,[100] 20 g of the carbon black (VFC-SP0450) was dipped into an aqueous solution of 500 mL deionized (DI)-water mixed with 20 g of citric acid (99.5%). The mixture was stirred continuously using a magnetic stirrer for 60 min at room temperature. A shorter treatment time resulted in a lower density of the functional groups, while a longer stirring time resulted in saturation. A washing and drying post-treatment process, including a heating step at 300 °C for 60 min, was needed to remove the residual citric acid. The presence of these active sites improves the adsorption of the precursor and enables the deposition of well-dispersed Pt NPs with a considerably higher density than those on the untreated carbon (Fig. 6a and b). Consequently, a higher Pt loading on the acid-treated carbon is achieved, resulting in not only a higher electrochemical active surface area (ECSA) but also an enhanced the charge transfer in the oxygen reduction reactions (ORR).[100] A pretreatment in concentrated nitric acid has been demonstrated to be efficient for the functionalization of Vulcan carbon black prior to Pt ALD.[103] Besides the formation of anhydride and carbonate surface groups, this treatment additionally generates monatomic oxygen and nitrogen attached to the surface, facilitating the adsorption of $MeCpPtMe_3$ (methylcyclopentadienyl trimethylplatinum), which is a commonly used organometallic Pt precursor for ALD, widely employed for the deposition of Pt thin films and NPs.[104] However, the treatment in concentrated acid may result in the removal of carbon from the surface, which causes a considerable decrease in the surface area.

For graphene surface, its inert nature hinders the adsorption of the precursor molecules. Therefore, ALD on this surface results in the deposition of Pt NPs mainly along the graphene edges and sporadically on the basal planes (Fig. 6c).[105] A pretreatment in ozone (O_3) at 200 °C in 30 min (*i.e.*, for a batch of 0.75 g graphene powder with a specific surface area of 150 m^2 g^{-1}) alters the surface, enabling a uniform deposition of Pt NPs across the entire surface of graphene (Fig. 6d).[105,106] It is found that the O_3-treatment not only generates O-containing functional groups on the surface but also removes the adventitious carbon species and surface contaminants, and the treatment does not cause any visible effect on the crystalline structure of the graphene.[105] Oxygen pretreatment can also be applied to enhance the nucleation of Pt ALD. A recent theoretical study by Le *et al.* reveals that this treatment can generate various defect types, such as single (C) vacancy, double vacancy without or with a chemisorbed oxygen atom or a hydroxyl group.[107] Among these defects, the divacancy with a chemisorbed oxygen atom is found to have the lowest free-energy structure, making it most favorable to form by the oxygen treatment. The divacancy plays a key role in enhancing chemical reactivity, accelerating the reaction rates during removal of the $MeCpPtMe_3$ ligands, while the chemisorbed oxygen atom stabilizes the divacant state. In comparison with the wet-chemistry approach, the O_3 pretreatment is more advantageous as it can be conducted in the gas phase in the same reactor,[105,106] enabling a faster process and avoiding the post-treatment steps encountered in the wet-chemistry process, such as washing, filtering, and drying.[100,101,103]

We note that while the surface pretreatments are highly effective for enhancing the surface reactivity and promoting the

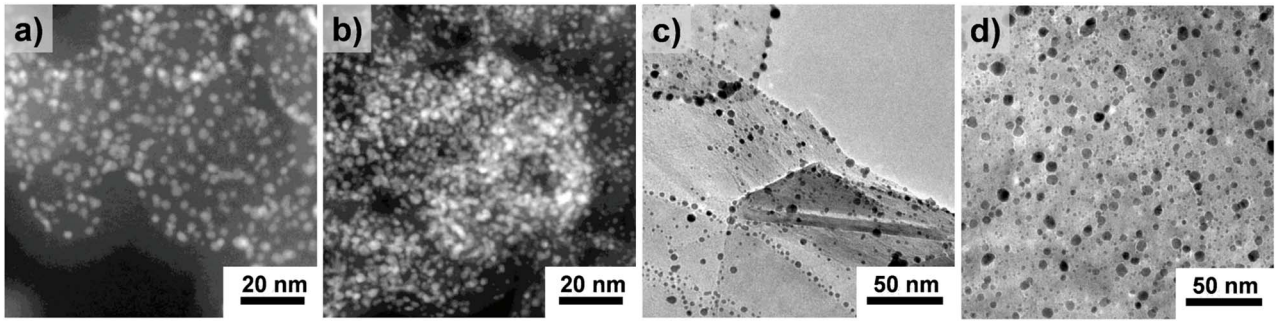

Fig. 6 TEM images of Pt NPs deposited on Vulcan XC 72 nanocarbon without (a) and with (b) the citric acid pretreatment. Adapted from ref. 100 with permission from Wiley, copyright 2022. Pt NPs deposited on graphene nanoplatelets without (c) and with (d) the O_3 pretreatment. Adapted from ref. 105 with permission Royal Society of Chemistry, copyright 2017.

precursor adsorption during the initial stages of ALD, the resulting surface functionalities are often metastable and may evolve over time. The thermal relaxation, the exposure to ambient conditions, or the subsequent processing steps can lead to partial decomposition or desorption of the oxygen-based groups, resulting in a gradual reduction in the surface reactivity. This temporal evolution can influence the reproducibility of ALD nucleation and may introduce variability if there is a prolonged delay between surface pretreatment and deposition. In the context of FB-ALD, however, these oxygen functionalities primarily act as temporary nucleation sites to facilitate the early adsorption of the precursor molecules. Once the nucleation is established, the continued ALD growth becomes less sensitive to the long-term stability of the initial surface groups. Nevertheless, this limitation emphasizes the importance of carefully controlling the pretreatment conditions and minimizing the storage time prior to ALD.

Size-controlled Pt NPs

Particle size distribution (PSD) and density are among the most critical factors influencing the catalyst performance.[108] Surface pretreatment can enhance the density and enable a uniform distribution of Pt NPs on the carbon supports, however, achieving a highly uniform particle size with a narrow PSD remains a major challenge. This difficulty arises from the complex growth mechanisms of Pt NPs, which involve multiple phenomena such as adsorption and reaction of the precursors,[109,110] diffusion and coalescence of NPs,[106] and Ostwald ripening.[111] Several studies have demonstrated that well dispersed Pt NPs with a high size-uniformity on carbon black can be achieved by ALD at 300 °C using $MeCpPtMe_3$ as the precursor.[99,101,103] Hence, the particle size and the Pt loading are controlled by the number of ALD cycles, in which a linear relation between the size and loading and the number of ALD cycles can be achieved.[101] A remarkable advantage of ALD is its ability to produce highly dispersed Pt NPs with reduced agglomeration on the support material. Hence, Pt NPs supported on carbon materials (Pt/C catalysts) synthesized by ALD commonly possess a considerably higher ECSA compared to commercial counterparts with equivalent Pt loading. For example, Lee *et al.* reported that ALD-synthesized Pt/C catalysts with a Pt loading of 41.20 wt% exhibited an average particle size of 3.0 nm and an ECSA of 66.61 $m^2\ g^{-1}$.[99] In comparison, commercial Premetek Pt/C catalysts at a similar Pt loading (40 wt%) showed an ECSA of 58.46 $m^2\ g^{-1}$ and a particle size of 3.4 nm. Similar trends have also been observed for Pt/C catalysts with lower Pt loading and various carbon supports. Hence, ALD-synthesized Pt/C catalysts commonly achieve enhanced membrane electrode assembly (MEA) performance, resulting in higher current and power densities.[99–101]

Among various precursors for Pt ALD, $MeCpPtMe_3$ is the most widely utilized due to its advantages of having high thermal stability and high reactivity.[104] Hence, ALD of Pt using this precursor can be conducted in a wide temperature range using various reactants, such as oxygen (O_2),[110,112] ozone (O_3),[113,114] and hydrogen (H_2).[103,115,116] Taking these advantages, Lubers *et al.* explored two ALD chemistries, *i.e.*, the combustion reaction using O_2 and the hydrogenation using H_2, of Pt ALD using $MeCpPtMe_3$ on Vulcan carbon XC72R powder pretreated with nitric acid.[103] The study revealed that the H_2-based process produced Pt NPs with a significantly higher dispersion (43.9%) and smaller particle size (2.6 nm) compared to those obtained for the O_2-based process (*i.e.*, 36.5% in dispersion and 3.1 nm in particle size) after the same number of ALD cycles.[103] Similar effects were observed for the Pt ALD on Al_2O_3 powder.[115] This demonstrates that the choice of ALD chemistry can provide a pathway for controlling the size of Pt NPs. Nevertheless, since H_2 is less reactive than O_2, the hydrogenation reaction is less effective in removing precursor ligands. As a result, the Pt loading on the Pt/C catalysts obtained from the H_2-based process is notably lower, reflecting a reduced precursor usage efficiency. Therefore, a trade-off exists between achieving nanoparticle size control and maximizing catalyst loading in the selection of precursor chemistry.

Compared with the conventional carbon black supports, graphene and its derivatives (*e.g.*, graphene oxides, graphene nanoplatelets) offer several advantages for the fabrication of metal-based electrocatalysts.[117,118] Their two-dimensional (2D) structure and exceptionally high specific surface area (SSA) allow for a high dispersion of metal NPs and provide a higher density of accessible active sites. In addition, the high electrical conductivity of graphene facilitates efficient charge transport

during electrochemical reactions, while its high chemical stability improves catalyst durability under electrochemical operating conditions. Therefore, graphene is considered as an excellent support for noble metal-based catalysts.[119,120] Pt NPs supported on graphene demonstrate outstanding performance in various electrochemical reactions, such as methanol oxidation reaction (MOR)[80] and oxygen reduction reaction (ORR),[121,122] indicating their great potential for fuel cell applications.[123–125] Consequently, there has been growing interest over the last decade in employing ALD to deposit Pt NPs onto graphene and its derivatives.[80,126–128] It has been demonstrated that, unlike the deposition of Pt NPs on Vulcan carbon black,[99,101,103] ALD of Pt NPs on graphene surfaces shows a strong dependence between deposition temperature and particle size within two distinct temperature ranges.[105,106] At temperatures of 150 °C or higher, deposition leads to Pt NPs with poor uniformity due to sintering, which occurs through the diffusion and coalescence of NPs during the oxygen exposure step.[106] In addition, the mobility of Pt NPs depends on both particle size and temperature, resulting in decreased uniformity at higher temperatures. At the same time, new particles are constantly formed in each cycle, resulting in PSDs with a persistent peak at the small-size side and gradual broadening as the number of cycles increases (Fig. 7).[105] Thus, particle size cannot be effectively controlled by simply adjusting the number of cycles at these temperatures.

In contrast, at temperatures of 100 °C or lower, NP diffusion and coalescence are strongly suppressed. As a result, Pt ALD on graphene in this temperature range produces NPs with greater size uniformity and a narrow PSD, which gradually shifts toward larger sizes as the number of ALD cycles increases. This enables precise control of Pt NP size through the number of ALD cycles. Therefore, achieving ALD-like precision in nanoparticle size requires low deposition temperatures.[105,106] Nevertheless, it is important to note that thermal Pt ALD using $MeCpPtMe_3$ and O_2 is typically performed at temperatures between 150 and 300 °C.[104] Employing O_3 in thermal ALD or H_2 plasma in plasma-assisted ALD enables deposition at 100 °C and even room temperature, respectively.[113,129] This suggests that the primary limitation in lowering the deposition temperature for Pt ALD with $MeCpPtMe_3$ and O_2 arises not from the precursor adsorption in the first half-reaction but from the ligand removal in the second half-reaction. Grillo *et al.* found that it is the O_2 exposure, defined as the product of exposure time and partial pressure, that plays the key role in the removal of the precursor ligands.[130] By providing a sufficiently high O_2 exposure, Pt sub-nanometer clusters can be deposited on TiO_2 nanopowders even at room temperature.[131] Therefore, the successful deposition of Pt nanoparticles on graphene at 100 °C or lower has been attributed to the extended exposure time (on the order of minutes) and the high O_2 partial pressure (0.2 bar),[105,106] which reflect a considerable benefit of the fluidized bed reactor operating at atmospheric pressure.

Composition-controlled Pt-based core–shell NPs and Pt-alloy NPs

The cyclic nature of ALD and, importantly, the surface selectivity of precursor adsorption allow for sequential deposition of different elements, enabling the controlled formation of well-defined nanostructured catalysts, such as core–shell[83–86] and alloy NPs.[87–89] Weber *et al.* demonstrated the synthesis of supported bimetallic Pd@Pt and P@Pd core–shell NPs entirely by ALD using $MeCpPtMe_3$ and $Pd(hfac)_2$ as the precursors for Pt and Pd, respectively.[84] For the deposition of Pd@Pt core–shell, Pd NPs were first deposited onto the substrate (*i.e.*, Al_2O_3) employing $Pd(hfac)_2$ and H_2 plasma at a substrate temperature of 100 °C. The formation of Pd NPs is promoted by the preferential Volmer–Weber growth of noble metals on oxide surfaces due to their surface energy differences.[132] In this manner, the size of the core particle can be tailored by varying the number of ALD cycles. In the next step, the experimental conditions for the subsequent Pt ALD were tuned to favor the selective chemisorption of $MeCpPtMe_3$ molecules on the surface of Pd NPs rather than on Al_2O_3. This was achieved by reducing the O_2 partial pressure to ~1 Pa. Under these conditions, no Pt growth was detected on Al_2O_3 even after 1000 ALD cycles, whereas a growth rate of ~0.45 Å per cycle was obtained on the Pd surface.[84] In the other direction, Pt-core NPs were deposited on Al_2O_3 substrate at an O_2 partial pressure of 100 Pa, while the subsequent deposition of the Pd shell was altered to the thermal ALD mode at 100 °C. This enables a dissociative chemisorption of H_2 on the noble metal surfaces and not on Al_2O_3, which consequently leads to the selective deposition of Pd on Pt NPs, resulting in the formation of Pt@Pd core–shell NPs.[84]

Taking the advantages of the selective deposition achieved by tailoring the deposition conditions, core–shell NPs of various noble metals such as Pt, Pd, Ru, and Au have been successfully realized by ALD.[15,83,133–136] For instance, Wang *et al.* demonstrated the fabrication of Au@Pd core–shell NPs supported on SiO_2 nanopowders by ALD of Pd using $Pd(hfac)_2$ as the precursor.[137] At 150 °C, the $Pd(hfac)_2$ exhibited selective adsorption on the Au surface, allowing Pd deposition exclusively on the Au nanoparticles. This enabled precise control of the Pd shell thickness down to a few angstroms, achieving strongly enhanced performance in the oxidation of benzyl alcohol over the its counterparts with single-element NPs.[137] Another approach to achieve selective deposition for core–shell NP fabrication involves the use of self-assembled monolayers (SAMs),[138,139] which can effectively inhibit the chemisorption of precursor molecules on specific regions of the substrate where they are applied. Cao *et al.* demonstrated a SAM-assisted area-selective ALD method to synthesize Pd@Pt and Pt@Pd core–shell NPs with precise control of size, shell thickness, and composition.[86] By modifying the substrate with octadecyltrichlorosilane (ODTS) SAMs, nanoscale pinholes were created, which functioned as nucleation sites for the core growth in the first ALD process. Subsequently, the deposition of shell by the second ALD process occurred exclusively on the core since the ODTS molecules blocked the new nucleation. This

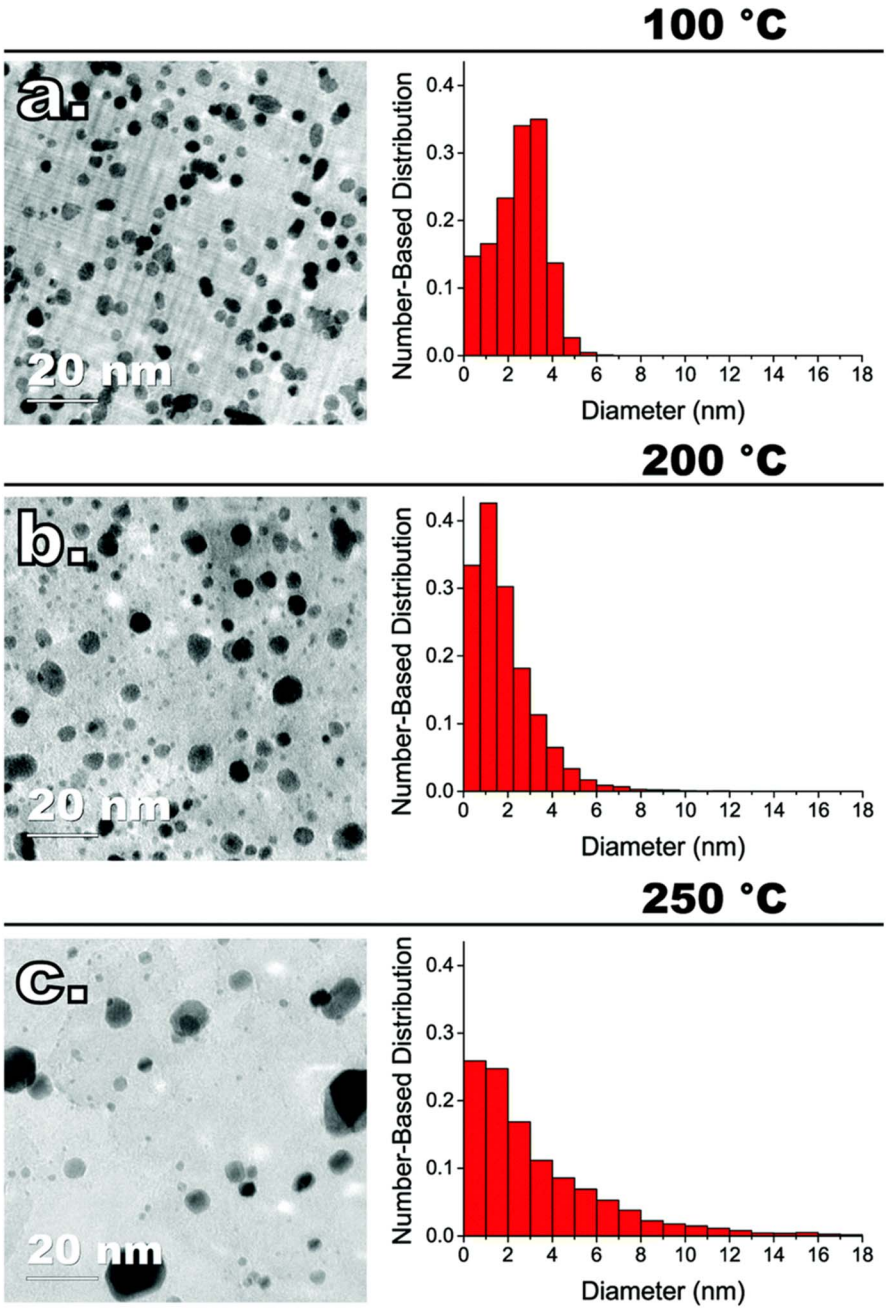

Fig. 7 TEM images of ALD-grown Pt NPs on graphene nanoplatelets after 10 cycles at 100 °C (a), 200 °C (b), 250 °C (c), and respective number-based PSDs. Adapted from ref. 105 with permission from the Royal Society of Chemistry, copyright 2017.

approach enables the fabrication of uniform core–shell NPs using standard ALD processes.

Making Pt-alloy NPs not only reduces the Pt loading but also offers enhanced activity, stability, and selectivity for various applications, such as fuel cells,[140,141] hydrogen oxidation reactions (HORs),[142,143] oxygen reduction reactions (ORR),[144–146] hydrogen evolution reactions (HERs),[143,147] and CO_2 reduction reactions.[148] By alloying Pt with other metals (*e.g.*, Ni, Co, Cu, Fe, Zn), the catalytic performance can be tuned through electronic and geometric effects, optimizing both reaction kinetics and durability. Traditional synthesis methods, including wet-chemical approaches,[148,149] physical vapor deposition,[150,151] and electrodeposition,[152,153] enable alloy formation but often suffer from poor compositional control and inhomogeneous distribution of elements due to the diverse nucleation and growth rates of different elements.[154] Therefore, achieving precise control of the composition and spatial distribution of metals remains a major challenge, especially when targeting sub-nanometer or atomically dispersed structures. In this context, ALD presents a promising alternative due to its unique ability to deposit metals with atomic-level precision, ensuring tunable

stoichiometry, and exceptional dispersion on high-surface-area supports.[155–158]

In general, a full-ALD approach for the synthesis of alloys is conducted using super-cycles composed of multiple ALD processes with a defined cycle ratio (*i.e.*, the super-cycle ratio).[10] This strategy is commonly used for depositing doped films and multi-layered structures.[159–162] The composition and the particle size of alloys are controlled by both the super-cycle ratio and the number of super-cycles. Following this approach, Lee *et al.* demonstrated the deposition of PtNi alloy NPs on carbon black by combining two ALD processes for Pt and Ni using FB-ALD.[87] The Pt ALD process employed $MeCpPtMe_3$ and O_2, while Ni ALD employed $Ni(dmamb)_2$ and H_2, with both processes conducted at 300 °C. The percentage of each metal in the PtNi alloy NPs was controlled by adjusting the super-cycle ratio from Pt : Ni = 5 : 1 to 1 : 5, while the total loading of the metals was controlled by the number of super-cycles, which was determined based on the total number of cycles of each metal ALD process. However, the differences in the initial growth and the deposition rate between the ALD processes can result in a non-monotonic relation between the cycle ratio and the atomic concentration of each element. Therefore, they must be investigated and taken into account when determining the appropriate number of super-cycles. By doing so, Lee *et al.* demonstrated the ability to tailor the atomic concentration of Pt in the PtNi alloy between approximately 75 and 85% and simultaneously the atomic concentration of Ni between 25 and 15% (Fig. 8a–d).[87] As deposited PtNi bimetallic NPs exhibited a low crystallinity and an oxidized state of Ni. Therefore, a heat treatment under a constant H_2 flow of 50 sccm at 700 °C for 1 h was applied. This step reduced the oxide state of Ni and enabled the formation of well-mixed PtNi alloy NPs, which caused a modification of crystalline structure and chemical bonding states as detected by the peak shift in the X-ray diffractograms and XPS spectra. However, this only caused a slight increase in the particle size (*i.e.*, 0.2 nm) and did not cause any considerable aggregation of the alloy NPs (Fig. 8e–h). On the contrary, the treatment in the same environment at 900 °C caused a severe coalescence, resulting in a noticeable increase in particle size. Importantly, the heat treatment of PtNi alloy NPs may cause the surface segregation of Pt atoms, creating a Pt skin layer surrounding the PtNi alloy core (Fig. 8i and j). This was observed for the PtNi alloy NPs with the higher Pt concentrations, as evidenced by the line profiling analysis shown in Fig. 8k and l. The formation of the Pt skin layer strongly enhanced the catalytic activity of the

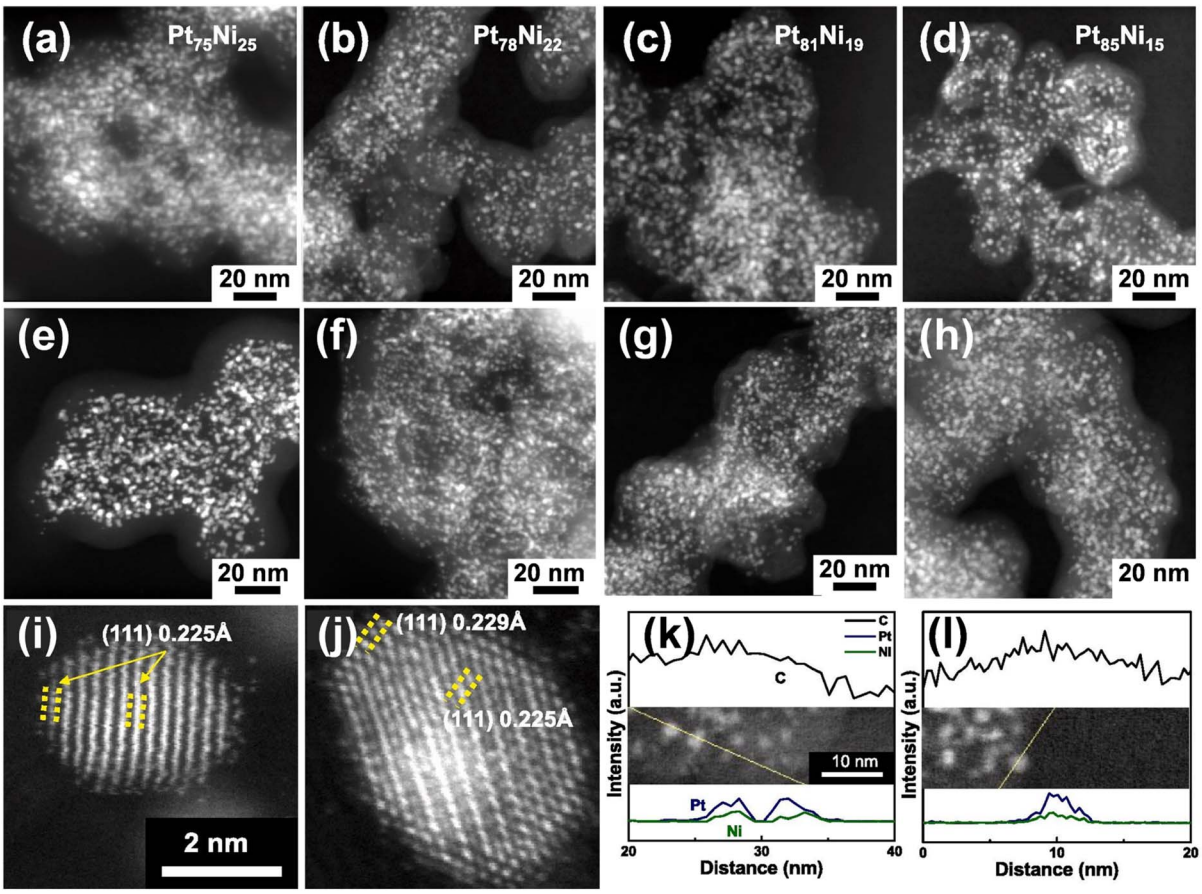

Fig. 8 HADDF-STEM images of as-deposited PtNi alloy NPs: (a) $Pt_{75}Ni_{25}$, (b) $Pt_{78}Ni_{22}$, (c), and $Pt_{81}Ni_{19}$ (d), and the corresponding PtNi alloy NPs after the heat-treatment with H_2 at 700 °C (e–h); high-magnification Cs-TEM images of $Pt_{75}Ni_{25}$ (i) and $Pt_{78}Ni_{22}$ (j), and the corresponding line profiling analysis of STEM mode for $Pt_{75}Ni_{25}$ (k) and $Pt_{78}Ni_{22}$ (l). Adapted from ref. 87 with permission from Elsevier.

catalysts, which exhibited not only outstanding ORR as well as PEMFC performances but also excellent durability.

A full-ALD approach using super-cycles consisting of alternating Pt and Pd ALD processes was also applied to deposit PtPd alloy NPs on Vulcan XC-72 carbon support.[163] This was performed in an FB-ALD system operating at atmospheric pressure. The Pt ALD process employed $MeCpPtMe_3$ and O_3. For each experiment with 0.5 g of carbon powder, a Pt ALD cycle consisted of 1 min dosing of $MeCpPtMe_3$, 5 min dosing of O_3 and 5 min purging by N_2 (99.999 vol%) after every precursor or reactant dose. The Pd ALD process used $Pd(hfac)_2$ and formalin, with the dosing times for the precursor, the reactant, and the purge time were 12 min, 6 min, and 12 min, respectively. The flow of N_2, which served as both the carrier and the purging gas, was fixed at 1 L min^{-1}. To assist the vaporization, the two precursors contained in stainless steel bubblers were heated to 70 °C. Both the Pt and the Pd ALD processes were carried out at 200 °C. Prior to the deposition, the carbon powder was functionalized by a pretreatment in O_3 at 200 °C for 30 min. The deposition of PtPd alloy NPs was performed for 3 super-cycles, each consisting of 1 cycle of Pt ALD followed by 4 cycles of Pd ALD. For comparison, the fabrication of both Pt@Pd core–shell and Pd@Pt core–shell NPs with the same total number of cycles of Pt ALD (3 cycles) and Pd ALD (12 cycles) were conducted. The study demonstrated the successful deposition of highly dispersed and uniformly distributed NPs of Pt/Pd and Pd/Pt core–shell structures as well as well-mixed Pt–Pd alloys, as indicated by the TEM images and the STEM-EDX elemental mappings shown in Fig. 9.[163] The average particle size for all three structures was around 8.6 nm. The Pt loading ranged from 2.11 to 2.57 wt%, while the Pd loading varied between 3.88 and 4.98 wt%, resulting in a total metal loading of 5.99 to 7.55 wt%. Both Pt and Pd loadings were highest in the alloy NPs. The variation in metal loadings, despite an equal number of ALD cycles, can be attributed to differences in the initial growth behavior of each metal on the carbon surface, as mentioned above. Nevertheless, the loading ratio between the two metals remained consistent at approximately 65 : 35 for all three structures. This reflects the ability to control not only the structure but also the elemental compositions of each structure using this all-ALD approach to tailor the material properties. In this particular case, the activity of the three catalysts was tested with the CO_2 reduction to formic acid. The results showed that the Pt–Pd alloy catalyst reached 46% faradaic efficiency at −0.2 V *vs.* RHE, while the Pd@Pt and the Pt@Pd core–shell catalysts exhibited significantly lower faradaic efficiencies, *i.e.*, 22% and 11%, respectively, under the identical testing conditions. These findings indicate the great advantage of precise structural control enabled by the full-ALD approach, allowing for the rational design of catalyst architectures that directly influence and enhance their electrochemical performance.

ALD can be combined with another material synthesis method to realize alloy NPs, which can be considered as a half-ALD approach. Huang *et al.* employed this approach to achieve highly controlled sub-3 nm PtZn-alloy NPs on Vulcan XC-72 carbon support, as described by the diagram in Fig. 10a.[89] In this case, Pt NPs were first deposited onto the carbon support by an impregnation reduction method, which was then coated by

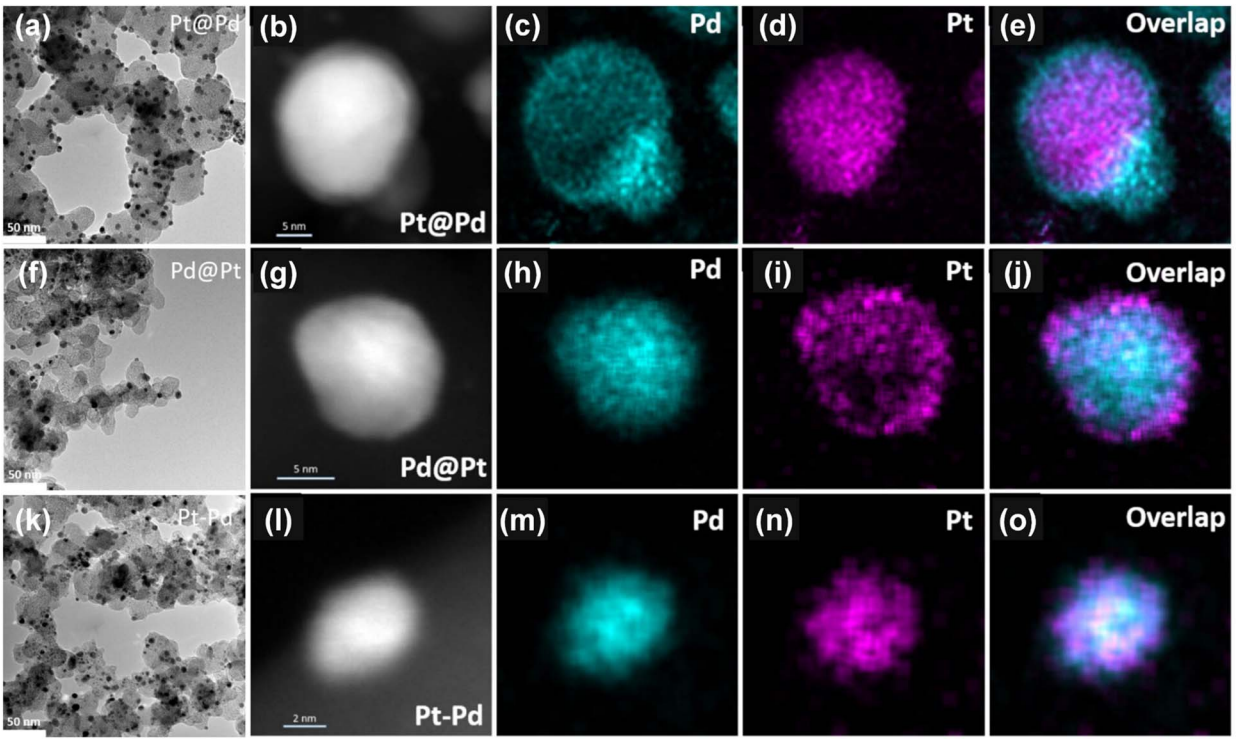

Fig. 9 TEM images and STEM-EDX elemental mappings of the Pt@Pd core–shell (a–e), Pd@Pt core–shell (f–j), and Pt–Pd alloy structure catalysts (k–o). Adapted from ref. 163 with permission from The Authors, copyright 2022.

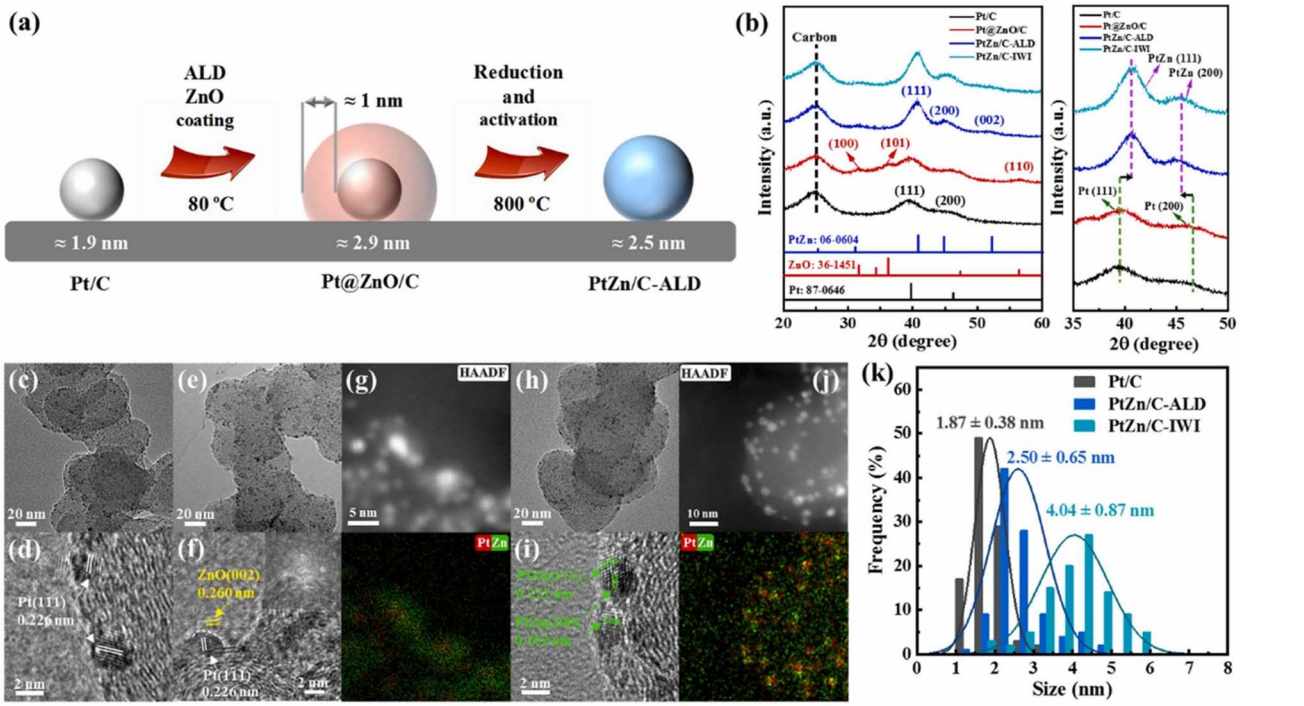

Fig. 10 Schematic diagram of synthesis process (a); XRD diffractograms and partial enlarged XRD diffractograms of the Pt/C by prepared by impregnation reduction method, the Pt@ZnO core–shell NPs on carbon (Pt@ZnO/C), the PtZn alloy NPs on carbon (PtZn/C-ALD) obtained after the H_2 treatment, and the PtZn alloy NPs on carbon obtained by incipient wetness impregnation (IWI) method (PtZn/C-IWI) (b); TEM image (c) and HR-TEM image (d) of Pt/C; TEM image (e) and HR-TEM image with corresponding fast Fourier transform image (f) of Pt@ZnO/C; HAADF-STEM image and elemental mapping of Pt@ZnO/C (g); TEM image (h) and HR-TEM image (i) of PtZn/C-ALD; HAADF-STEM image and elemental mapping of PtZn/C-ALD (j); PSDs of Pt/C, PtZn/C-ALD and PtZn/C-IWI (k). Reproduced from ref. 89 with permission from Elsevier, copyright 2022.

ZnO films by ALD. To achieve a selective deposition of ZnO exclusively on Pt NPs, the as-synthesized Pt/C was reduced by diluted H_2 (*i.e.*, 10% H_2 in Ar) at 600 °C for 1 h to eliminate surface hydroxyl groups and prevent the ZnO deposition on the carbon support. In addition, O_2 was selected as the oxygen source for ZnO ALD using diethylzinc, and the deposition temperature was maintained at 80 °C to ensure that the activation occurred exclusively on Pt NPs. The ZnO shell thickness can be precisely controlled by adjusting the number of ALD cycles. Subsequently, the Pt@ZnO core–shell NPs (Pt@ZnO/C) was converted into alloy by a rapid annealing in diluted H_2 (*i.e.*, 10% H_2 in Ar) at 800 °C with a heating rate of 5 °C min^{-1} for 1 h, which reduced the oxide state and facilitated the diffusion of Zn atoms into the lattice of Pt. This caused a contraction of the Pt lattice, resulting in a noticeable peak shift in the XRD diffractograms (Fig. 10b). The TEM images indicate the successful deposition of Pt NPs on the carbon support (Pt/C, Fig. 10c and d), the Pt@ZnO/C NPs (Fig. 10e–g), and the PtZn alloy NPs (PtZn/C-ALD, Fig. 10h–j). The core–shell and the alloy structures are evidenced by the elemental mapping shown in Fig. 10g and j. Despite experiencing a heat treatment at 800 °C, no particle aggregation was observed, indicating a high sinter-resistance and high stability of the PtZn alloy NPs. As demonstrated by the PSDs shown in Fig. 10k, the particle size of the PtZn alloy NPs realized by ALD is significantly smaller and the PSD is narrower than those for the PtZn alloy NPs synthesized by incipient wetness impregnation method (PtZn/C-IWI).

The capability of precisely controlling the growth of PtZn alloy NPs translates into an exceptional catalytic performance in oxygen reduction reactions of the PtZn/C-ALD catalyst, which outperforms the synthesized Pt/C, Pt@ZnO/C, PtZn/C-IWI, and even the commercial Pt/C catalysts.[89] For instance, the mass activity and the specific activity of PtZn/C-ALD reached 0.60 A mg_{Pt}^{-1} and 1.06 mA cm^{-2}, which were 6.0 and 6.8 times higher than those of the commercial Pt/C catalyst (0.10 A mg_{Pt}^{-1} and 0.15 mA cm^{-2}). In addition, the PtZn/C-ALD catalyst showed a smaller Tafel slope (50 mV dec^{-1}) compared to the commercial Pt/C catalyst (56 mV dec^{-1}), while the H_2O_2 yield during ORR catalyzed by PtZn/C-ALD was 1–2% lower than that of the commercial Pt/C. Notably, the PtZn/C-ALD catalyst exhibited outstanding stability and durability after an accelerated test. Specifically, the PtZn/C-ALD only showed a slight decrease in ECSA from 59.43 to 55.16 m^2 g_{Pt}^{-1} after 30 000 cycles, whereas the commercial catalyst exhibited a significant loss from 63.69 to 34.70 m^2 gPt^{-1} after only 10 000 cycles. The mass activity of the PtZn/C-ALD after 10 000 and 30 000 cycles was 0.46 A mg_{Pt}^{-1} and 0.35 A mg_{Pt}^{-1}, respectively, while the mass activity of the commercial Pt/C was 0.03 A mg_{Pt}^{-1} after 10 000 cycles. Moreover, after 300 cycles of the acceleration duration test, the average size of PtZn/C-ALD NPs showed an increase from 2.50 to 3.01 nm while its PSD remained substantially narrow. In

contrast, the commercial Pt/C catalyst failed to hold its size and PSD with a severe increase in size and broadening in distribution. It was found that the formation of the alloy enhanced the interaction between the two metals, which consequently reduced the binding energy of Pt-oxygen intermediates, leading to the enhancement of the catalytic activity. In addition, the electrochemical Ostwald ripening of Pt in the ALD-synthesized PtZn/C catalyst was strongly suppressed, which consequently enhanced the stability and durability of the catalyst. This approach demonstrates the strong potential of ALD for producing robust fuel cell catalysts and has also been applied to synthesize PtSn alloy NPs on carbon, which exhibit excellent performance in oxygen reduction reactions (ORR).[164]

Stability-controlled Pt NPs

Controlling the stability of catalysts is essential for ensuring sustained activity and efficiency during long-term operation, particularly in demanding environments such as high-temperature reactions, corrosive media, or electrochemical systems. Catalyst deactivation can occur through various mechanisms, such as poisoning, coking, sintering, leaching, solid-state transformation, and electrochemical Ostwald ripening, all of which contribute to the loss of active sites and structural degradation.[165–168] To address these challenges, several strategies have been developed, such as alloy formation to strengthen interatomic bonds,[169,170] core–shell architectures to confine active metals,[171,172] and protective surface coatings to minimize the degradation.[173,174] In this regard, ALD stands out as a highly effective approach, providing numerous surface engineering pathways for the design of highly stable catalysts by selectively depositing protective layers or tailoring the composition and structure at the atomic scale. As previously discussed, alloy NPs synthesized *via* either a full-ALD or a half-ALD process not only enhanced the catalytic activity but also improved the stability compared to the single-element and core–shell NPs.[89,163,164] This makes alloying one of the most effective strategies for boosting the stability and durability of electrochemical catalysts. In the following section, we explore two additional ALD-based approaches: the deposition of protective surface coatings and the addition of catalytically active NPs.

Surface coating *via* ALD has been widely adopted for improving the stability of catalysts and various energy materials, owing to its ability to precisely control film thickness at the atomic scale, which is an essential factor for maintaining an optimal performance.[175–181] In addition, ALD provides a broad selection of coating materials and operates over a wide range of deposition temperatures, making it especially advantageous for protecting active components and heat-sensitive substrates. Among the various protective coating materials, Al_2O_3 is the most widely used due to its well-developed ALD process and the exceptional reactivity of trimethylaluminum (TMA), the most established precursor for Al_2O_3 ALD.[182] TMA can be used in conjunction with H_2O, O_2 or O_3, enabling the Al_2O_3 even at room temperature with the thickness control at the sub-nanometer level.[176,183,184] Therefore, ALD of Al_2O_3 has been applied to improve the stability of Li-ion battery materials,[176,177,185] Li–S battery materials,[180] solid oxide fuel cell materials,[175] phosphors,[184,186] and many other active materials.[187,188]

Alternatively, Lee *et al.* proposed a strategy to enhance the stability of Pt/C fuel cell catalysts by applying an *in situ* TiO_2 protective layer *via* ALD.[189] In this approach, Pt NPs were first deposited on carbon black by ALD using $MeCpPtMe_3$ and O_2 at 300 °C.[99,101] Directly after the Pt deposition, a TiO_2 coating was applied using titanium tetraisopropoxide (TTIP) and H_2O at 250 °C in the same reactor, producing the TiO_2/Pt/C catalyst. For comparison, the reverse sequence, *i.e.*, TiO_2 deposition prior to Pt ALD, was also explored, resulting in the Pt/TiO_2/C catalyst. In both cases, the number of Pt ALD cycles was 15, whereas that of the TiO_2 ALD was 10. Remarkably, the difference in total loading of Pt and TiO_2 in both cases was insignificant, which approximately equaled the sum of the loadings obtained for each individual ALD process of Pt and TiO_2. STEM images and elemental EDS mapping of the two catalysts are shown in Fig. 11a and b.[189] For the Pt/TiO_2/C catalyst, TiO_2 was found to form thin films on the carbon surface, as clearly evidenced by the uniform distribution of Ti atoms in the EDS mapping image shown in Fig. 11c. The subsequent Pt ALD process yielded well-dispersed Pt NPs on the TiO_2 surface, as indicated by the STM image (Fig. 11a) and the EDS mapping for Pt (Fig. 11b). In the reverse sequence, ALD of Pt on carbon also resulted in highly dispersed Pt NPs on the carbon surface (Fig. 11e and f). Remarkably, the followed TiO_2 ALD process enabled the selective growth of TiO_2 only on the Pt NPs, as indicated by the EDS mapping of Ti shown in Fig. 11g. This forms a shell layer that strongly enhanced the stability and durability of the catalyst, which were investigated by both the accelerated degradation and the MEA durability tests for TiO_2/Pt/C, Pt/TiO_2/C and a commercial Pt/C catalyst with an equivalent Pt loading.

Although the TiO_2/Pt/C catalyst exhibited a slightly lower ECSA compared to Pt/TiO_2/C and the commercial Pt/C, which is likely due to partial coverage of active sites or reduced conductivity from the TiO_2 shell, its ECSA remained remarkably stable, even showing a slight increase after 10 000 cycles of accelerated degradation test (Fig. 11i). In contrast, both Pt/TiO_2/C and the commercial Pt/C suffered a considerable ECSA loss, with the commercial catalyst declining by over 36%. A similar trend was observed in MEA durability tests (Fig. 11j). While the TiO_2/Pt/C catalyst initially showed slightly lower current density, it maintained high stability after 20 000 cycles. The Pt/TiO_2/C catalyst remained stable up to 10 000 cycles but declined thereafter, whereas the commercial catalyst showed a steady current drop at every measured point. Moreover, the post-test PSD analysis (Fig. 11k–p) showed that the Pt NPs in the TiO_2/Pt/C catalyst were less affected, maintaining a smaller size and a narrower distribution. In contrast, both Pt/TiO_2/C and commercial Pt/C exhibited noticeable particle growth and broader distributions. These results indicate the crucial role of ALD-deposited TiO_2 layers in enhancing the long-term stability of Pt/C catalysts.

Ultra-thin SiO_2 films deposited by ALD using $SiCl_4$ and H_2O have also been proven to be an effective protective layer for improving the durability of Pt/C catalysts.[190] Notably, SiO_2 ALD

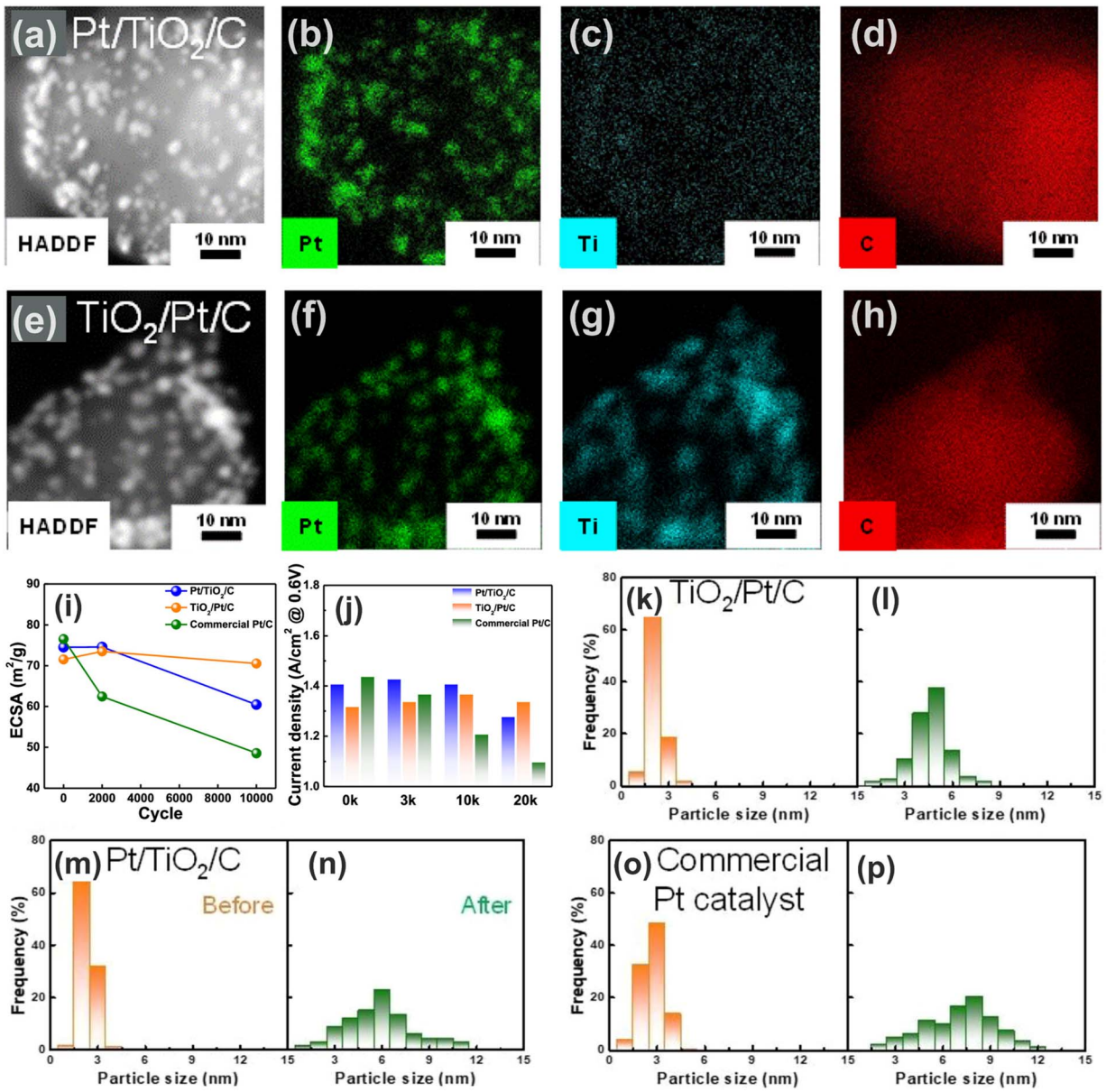

Fig. 11 STEM and EDS mapping images of Pt, Ti, and C elements for the $Pt/TiO_2/C$ (a–d) and $TiO_2/Pt/C$ (e–h) catalysts; evolution of the calculated ECSA of $Pt/TiO_2/C$, $TiO_2/Pt/C$, and the commercial Pt/C catalysts measured at the initial cycle and after 2000 and 10 000 cycles of the accelerated degradation test (i); current density measured at the initial cycle, and after 3000, 10 000, and 20 000 cycles of the MEA durability tests (j); PSDs of Pt NPs before and after the accelerated degradation test for $TiO_2/Pt/C$ (k and l), $Pt/TiO_2/C$ (m and n) and the commercial Pt/C catalyst (o and p). Adapted from ref. 189 with permission from American Chemical Society, copyright 2022.

using $SiCl_4$ can be performed at relatively low temperatures, expanding its potential for broader applications.[191] Li *et al.* applied SiO_2 coating on a commercial Pt/C catalyst (40 wt% of Pt on Vulcan XC 72R carbon black) to prevent deactivation during water electrolysis.[190] The coating was performed in a fluidized bed reactor operating at atmospheric pressure at 100 °C, at which the growth-per-cycle of SiO_2 is expected to be approximately 0.5 Å.[191] The results showed that without the SiO_2 coating, the Pt/C catalyst suffered a 34% drop in current density at −0.2 V *vs.* RHE after an accelerated degradation test for 1000 cycles. In contrast, coating the catalyst with only 2 ALD cycles of SiO_2 reduced this loss to 7%, and with 5 cycles, the decrease was only 2%. The average Pt particle size increased by 16% after the accelerated durability test (ADT) in the uncoated catalyst, but only by 3% when protected with 5 ALD cycles of SiO_2. Moreover, a substantial Pt detachment was observed in the uncoated sample, with the Pt concentration in the electrolyte reaching 8.9 mg L^{-1} post-ADT. This detachment was substantially mitigated by the ALD-deposited SiO_2, reducing Pt dissolution by 80%. It is important to note that a thicker SiO_2 layer obtained after 20 ALD cycles can hinder the electron transfer, thereby suppressing the catalytic activity. These results confirm that ultrathin SiO_2 films, applied by only a few ALD cycles, can effectively suppress Pt agglomeration and leaching under harsh

electrochemical conditions without compromising catalytic activity.

While surface coatings can strongly enhance catalyst stability by preventing sintering, dissolution, and particle detachment, they are not a universal solution. In particular, oxide coatings are generally ineffective against carbon deposition (*i.e.*, coking), which is a major cause of catalyst deactivation in hydrocarbon processing and reforming reactions.[192,193] Although in several cases, surface coating exhibits anti-coking effect.[194,195] it is often more effective to engineer the surface with catalytically active NPs that can suppress coke formation or even gasify coke precursors instead of simply protecting the catalyst. ALD provides a powerful approach for this purpose, enabling the controlled deposition of ultrasmall, well-dispersed catalytic NPs that help mitigate coking while preserving or enhancing catalytic performance. This was demonstrated by the recent study by Zhao *et al.* who applied ALD to deposit a trace of Fe on the surface of Ni/Al_2O_3 catalysts to enhance the anti-coking performance and improve the catalyst stability.[88] In particular, the Ni/Al_2O_3 powder catalysts were prepared by incipient wetness impregnation, and Fe NPs were deposited by FB-ALD at 180 °C using $Fe(C_5H_5)_2$ and O_3. In this manner, the Fe loading was precisely controlled by the number of ALD cycles, which was a key factor to control the performance of the catalysts. In this ALD process, O_3 can effectively oxidize and remove the organic ligands of the Fe precursor, while also generating new active oxygen sites for chemisorption in the subsequent ALD half-cycle.[88] Alternatively, Fe can be deposited by using $Fe(C_5H_5)_2$ and H_2, as demonstrated by Wang *et al.*, enabling the deposition of Fe single atoms.[196] It was found that the presence of Fe with a trace loading (0.3–0.6 wt%) strongly enhanced the reduction of NiO oxide on the catalyst surface into the Ni^0 metallic state. This resulted in more accessible Ni^0 active sites for the catalytic reaction, thereby enhancing the catalytic performance in the dissociation of CH_4. Additionally, adding Fe promoted the activation and dissociation of CO_2 on Ni^0, resulting in a continuous formation of oxygen active species (CO* and O*) that oxidize CH_x species from the CH_4 decomposition, thus suppressing coke formation. As a result, Ni/Al_2O_3 catalysts modified with just 0.3 wt% Fe showed no performance degradation over a 72-hour stability at the severe coke temperature (650 °C). Moreover, the Fe addition boosted the CH_4 conversion by 14.3% at 600 °C, indicating an improved catalytic activity at low temperatures.[197] This approach demonstrate great potential of ALD to engineer coke-resistant catalysts with enhanced activity and long-term stability through precise surface modification with active NPs, which has recently been further demonstrated for the enhancement of coke resistance of Ni/Al_2O_3 catalyst by adding a substantially small amount of Pt by ALD.[170]

Applications of ALD in pharmaceuticals

ALD has recently gained traction in pharmaceutical research as a versatile surface modification technique. By enabling the precise engineering of nanoscale coatings, ALD can help solving long-standing challenges in drug formulation, delivery, and stabilization. One of the most well-established pharmaceutical applications of ALD is in controlling drug release profiles. By depositing ultrathin ALD films of metal oxides such as Al_2O_3, TiO_2, or SiO_2, the dissolution rate of active pharmaceutical ingredients (APIs) can be modulated.[198] These nanoscale films act as diffusion barriers, allowing for extended- and delayed-release formulations.[199–202] Importantly, the coating thickness can be tuned with sub-nanometer precision to meet specific therapeutic needs. Building on this, a groundbreaking application of ALD in the development of single-dose and delayed-release vaccines have been demonstrated.[203–206] By encapsulating antigen-containing powders with ALD-grown Al_2O_3 shells, the kinetics of the antigen release and antibody response can be controlled ranging from weeks to months, and the thermostability of the vaccines can be strongly enhanced.[203–206] ALD also plays a crucial role in tailoring the physical properties of pharmaceutical powders. Many drug substances suffer from poor flowability, agglomeration, or incompatibility with manufacturing processes. ALD coatings can be used to modify surface energy and alter physical properties such as moisture resistance, hydrophilicity, hydrophobicity, wettability, and electrostatic surface charge,[207–212] which can improve stability, enhance powder dispersion, prevent particle agglomeration, and enhance handling during manufacturing steps such as blending, granulation, or tableting. In addition, ALD has been applied to stabilize amorphous solid dispersions (ASDs), a widely used strategy for enhancing the solubility of poorly water-soluble drugs.[213,214] ASDs are prone to phase separation and recrystallization due to their thermodynamic instability.[215] ALD coatings on ASD particles can create effective moisture barriers and physical confinement, thereby preventing the crystallization and preserving the amorphous state.[200,216–218] This results in improved shelf-life and sustained bioavailability, addressing one of the major limitations of ASD-based drug products. In this section of the review, we discuss recent advancements in the application of ALD for controlling drug release, modifying surface properties, and enhancing the stability of APIs and ASD systems.

Controlled release of pharmaceuticals

Pioneering research on the application of ALD for pharmaceutical coatings was reported in mid-2017 by Kääriäinen *et al.*, who demonstrated that nanometer-scale coatings of Al_2O_3, TiO_2 or ZnO on acetaminophen powders substantially slowed the dissolution rate and altered the drug release profile without affecting its molecular identity and polymorphic structure.[198] For example, uncoated acetaminophen dissolved completely in phosphate-buffered saline (PBS, pH 6.8) at 37 °C within 2 minutes, whereas the samples coated with Al_2O_3 for 50 ALD cycles exhibited a prolonged release, extending up to 15–20 minutes before reaching a saturation. Zhang *et al.* also observed an extended release for lactose powders coated with Al_2O_3 after 14 ALD cycles, which corresponded to a thickness of 3.85 ± 0.94 nm.[202,219] Notably, this ALD-based strategy even enabled the design of delayed-release formulations, as demonstrated for budesonide powders coated by a thin Al_2O_3 layer.[202] These early

findings revealed the potential of ALD in modulating drug release, paving the way for subsequent studies in the field.

A notable achievement in application of ALD for pharmaceutical controlled release was reported by Hellrup *et al.*, who conducted the first pharmacokinetic study of ALD-coated drugs.[220] This was demonstrated with Al_2O_3-coated indomethacin, a nonsteroidal anti-inflammatory drug (NSAID) with analgesic and antipyretic properties.[221] The deposition employed TMA and H_2O, which was conducted in a Picosun SUNALE™ R-series ALD-reactor at 50 °C. It was found that ALD using a multi-step approach, in which the coating process was divided into a number of sets of ALD cycles, and the particles were deagglomerated by manual agitation between the ALD sets, not only prevented the agglomeration of the pharmaceutical powder (Fig. 12a) but also resulted in highly uniform and pinhole-free nanoshells (Fig. 12b). By doing so, after 115 ALD cycles (5 ALD sets), an Al_2O_3 film with a thickness of 30 nm was achieved. Importantly, the coating did not cause any observable change in crystal form or crystallinity of the drug (Fig. 12c). In addition, the ALD approach allowed for a considerably higher drug loading, *i.e.*, up to 82.4 ± 1.4 w%, indicating great potential for controlled release of long-acting injectable formulations. The *in vitro* dissolution tests showed that under identical experimental conditions, the uncoated indomethacin was completely dissolved within 5 min, while the coated indomethacin released only 16% of the API after 4 h. For the *in vivo* tests, a 12-week single-dose preclinical study was conducted in rats to compare uncoated and Al_2O_3-coated indomethacin. No rats were prematurely terminated or showed negative symptoms, indicating that the Al_2O_3-coated indomethacin was safe and well tolerated at doses up to 100 mg kg^{-1}. Blood samples (~0.2 mL) were collected at predose and after different time intervals of the administration. As indicated by the plasma concentration–time curves for indomethacin following the subcutaneous administration (Fig. 12d and e), the plasma levels of indomethacin in the rats administered with uncoated indomethacin decayed rapidly within 1 week, while all the Al_2O_3-coated indomethacin samples exhibited a sustained release and achieved a steady-state drug release after approximately one week. By assuming a steady-state release, the duration of the drug release from the depot at doses of 10 and 100 mg kg^{-1} was estimated to be approximately 16 and 52 weeks, respectively.[220] The results demonstrate a great potential of ALD for the development of sustained release formulations for long acting depot treatments, which has recently been demonstrated by Nanexa AB (Sweden), showing positive clinical data of the sustained-release formulation of liraglutide with one-month release.[222] This emphasizes the growing translational value of ALD as a versatile platform for engineering next-generation injectable therapeutics with extended release profiles.

Another notable advancement in this area was reported by La Zara *et al.*, who demonstrated the dual benefits of ALD in prolonging drug release and enhancing aerosolization of carrier-free budesonide dry powders for inhalation therapy.[199] In that

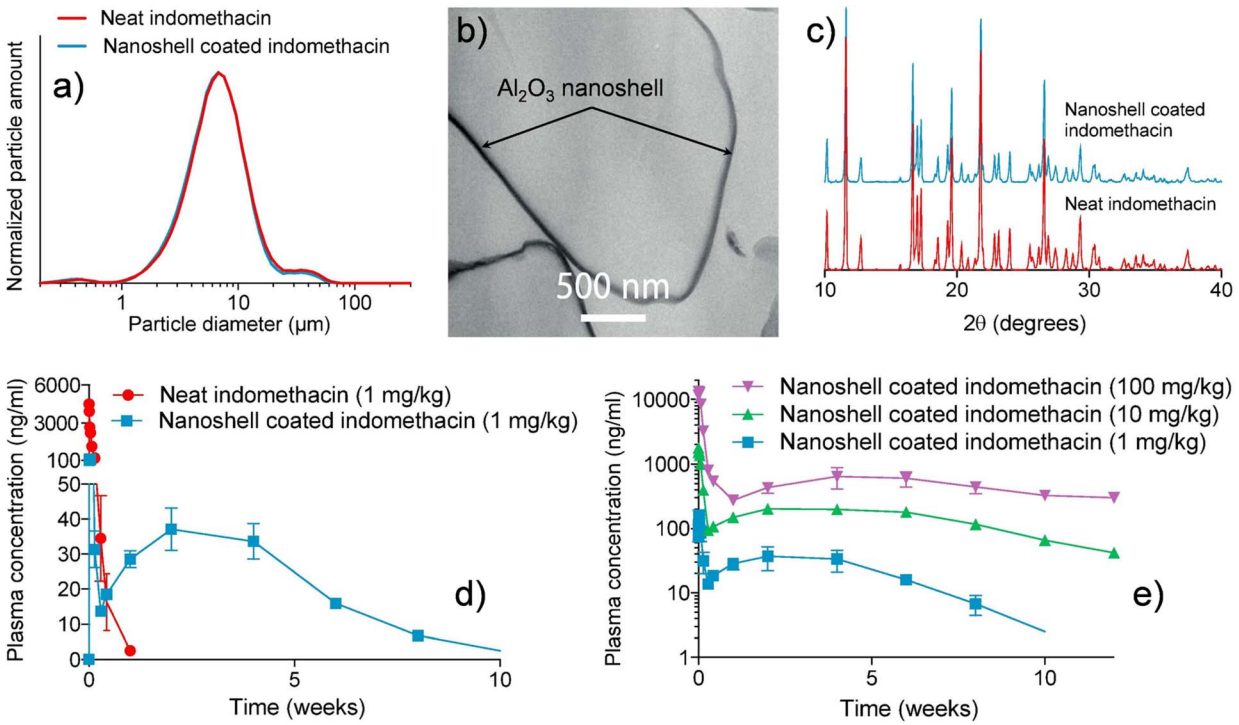

Fig. 12 (a) Size distribution analysis of neat indomethacin and Al_2O_3-coated indomethacin measured by laser light scattering; (b) TEM image of a Al_2O_3-coated indomethacin particle showing the nanoshell distribution surrounding the particle; (c) X-ray diffractograms of the uncoated and Al_2O_3-coated indomethacin. (d and e) Plasma concentration–time curves for indomethacin following subcutaneous administration, as measured by HPLC-MS/MS on blood plasma from test animals at different times. Reproduced and adapted from ref. 220 with permission from Elsevier, copyright 2019.

study, thin films of Al_2O_3, TiO_2, and SiO_2 with the thickness in the range of 3–50 nm were deposited on micronized budesonide particles using a fluidized bed ALD reactor operating at near-ambient conditions. Trimethylaluminum (TMA), titanium tetrachloride ($TiCl_4$) and silicon tetrachloride ($SiCl_4$) were used as the precursors for the deposition of Al_2O_3, TiO_2, and SiO_2, respectively, while O_3 (for Al_2O_3) and H_2O (for TiO_2 and SiO_2) were used as the co-reactants. Under these experimental conditions, the growth per cycle (GPC) obtained for the ALD TiO_2 and SiO_2 was found to be 0.1 nm and 0.3 nm, respectively. For the deposition of Al_2O_3, it was observed that during the coating process, the TMA precursor infiltrated the drug particles, leading to subsurface growth and the formation of a mixed Al_2O_3–budesonide layer near the particle surface, resulting in an undefined GPC for the ALD of Al_2O_3. Nevertheless, all the ALD processes resulted in uniform and conformal coatings of the oxide films on budesonide particles, as indicated by the TEM images and the EDX mapping shown in Fig. 13. *In vitro* and *ex vivo* tests confirmed that increasing the coating thickness consistently slowed the drug release, independent of the coating material, with Al_2O_3-coated particles showing the most sustained profiles.[199] This thickness-dependence provides the ability to tailor the release rate of the drug by controlling the number of ALD cycles. In addition, it was revealed that the coated particles remained largely intact during dissolution, suggesting a diffusion-based release mechanism through the ALD films. Importantly, fine particle fraction (FPF), which is a key metric for pulmonary delivery, was considerably improved, with up to a 2.3-fold increase observed for ALD-treated formulations compared to uncoated budesonide. This enhancement was attributed to reduced interparticle forces due to the oxide coatings, as confirmed by atomic force microscopy. Importantly, ALD-treated particles showed no cytotoxicity and retained anti-inflammatory efficacy in both 2D and 3D lung cell models, supporting their safety and therapeutic potential. The study provides compelling evidence that ALD is a highly effective approach for engineering inhalable drug powders with controlled release and superior delivery performance.

The capability of modulating the dissolution and release profiles of small-molecule drugs has extended the application of ALD into the field of vaccine, demonstrating a promising strategy to address challenges associated with multi-dose immunization schedules and cold-chain storage requirements. This emerging direction takes the advantages of the ability of ALD to deposit ultrathin, conformal layers of Al_2O_3 on antigen-loaded, spray-dried microparticles, enabling delayed antigen release and thereby mimicking a prime-boost response in a single injection.[203–206] Importantly, these Al_2O_3-coated formulations offer long-term thermostability, making them particularly attractive for global health initiatives in low-resource settings. A notable early study in this area was conducted by Garcea *et al.*,[203] who developed a single-administration vaccine against human papillomavirus (HPV) by combining spray drying of HPV16 L1 capsomeres with ALD coating using Al_2O_3 (Fig. 14a and b). The coating process was performed in a fluidized bed reactor at 70 °C and a low pressure (~300 Pa) using TMA and H_2O as the precursor and reactant, respectively. Under these conditions, a growth rate of

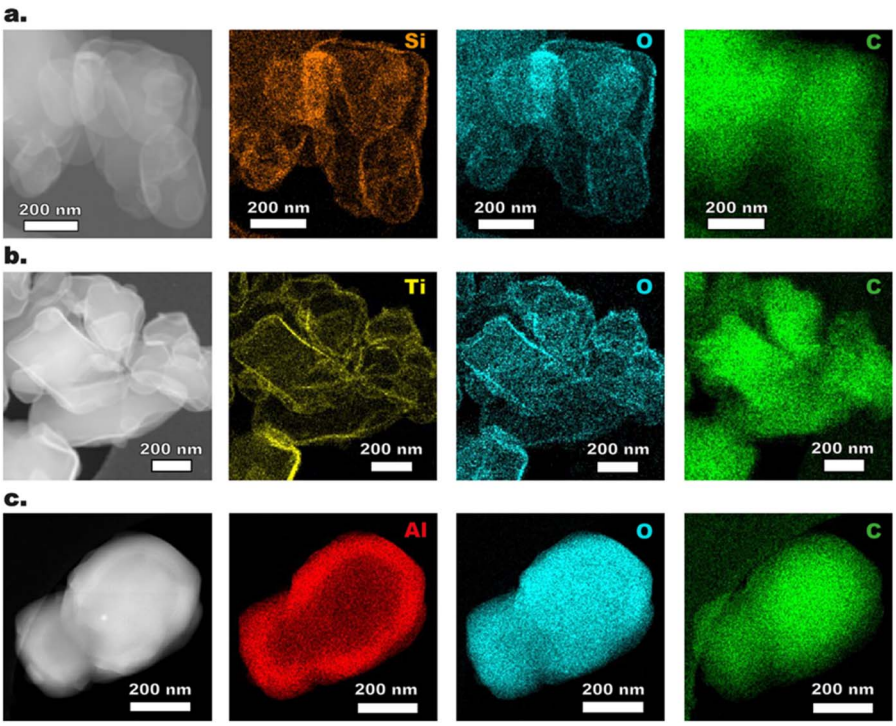

Fig. 13 High-angle annular dark-field (HAADF) images and EDX mappings of (a) Si, O, and C in SiO_2-coated budesonide after 100 cycles, (b) Ti, O, and C in TiO_2-coated budesonide after 50 cycles, and (c) Al, O, and C in Al_2O_3-coated budesonide after 50 cycles. Increasing film thickness results in slower dissolution rates for each ALD material. Reproduced from ref. 199 with permission from The Authors, copyright 2021.

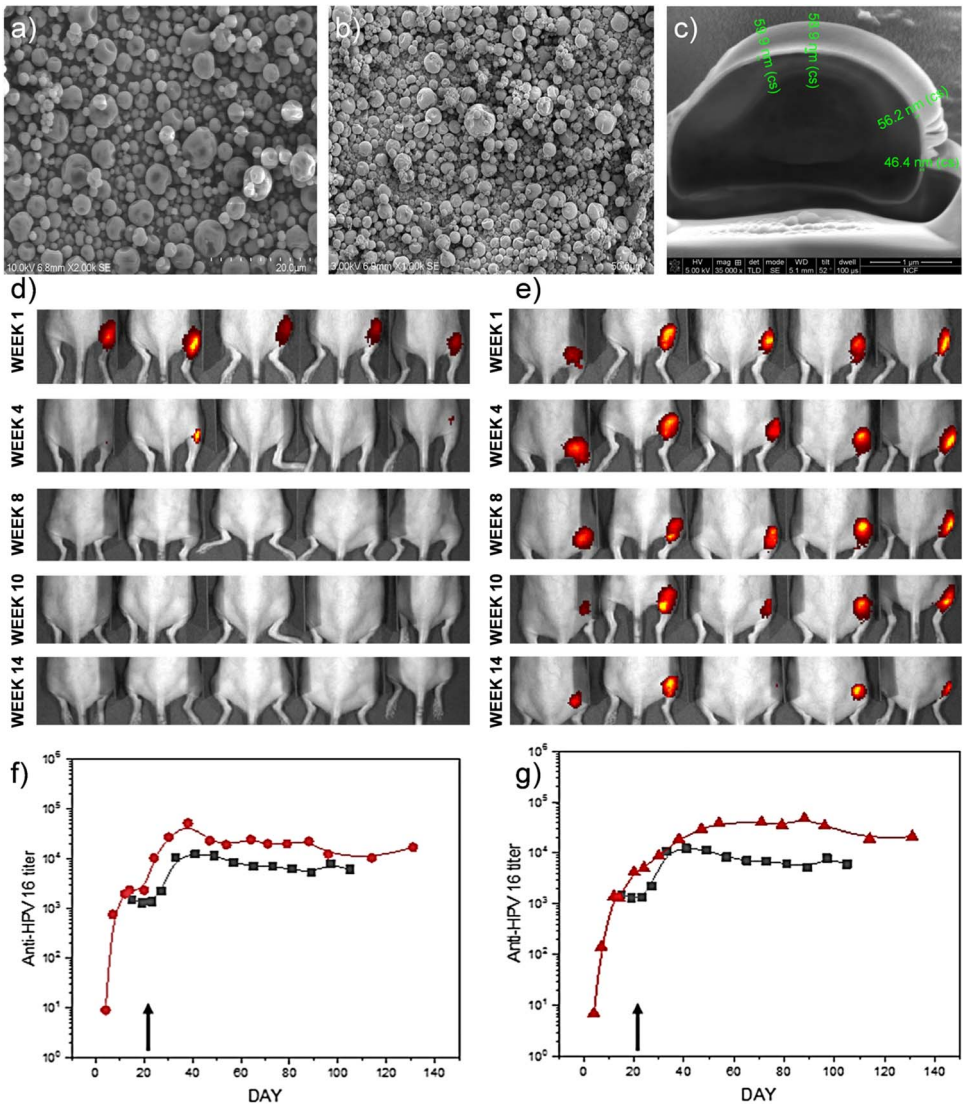

Fig. 14 SEM images of pray-dried, antigen-loaded microparticles (a) before and (b) after coating with Al_2O_3 for 250 ALD cycles with a growth-per-cycle of 2.3 Å; (c) TEM image of particles after coating with Al_2O_3 for 250 ALD cycles. Fluorescent images of SKH1 mice recorded at weeks 1, 4, 8, 10, and 14 following injection into their right dorsal thigh (d) with 5 μg of HPV16 L1 that was labeled with IRDye 800CW and adsorbed to alum prior to spray-drying but not coated and (e) with 5 μg HPV16 L1 that was labeled with IRDye 800CW, adsorbed to alum, spray-dried and coated with Al_2O_3 for 250 ALD cycles. Total anti-HPV16 antibody titers measured by enzyme linked immunosorbent assays (ELISA): (f) 5 μg prime/boost on days 0/21 with a suspension of HPV16 L1 capsomeres adsorbed on alum (indicated by black arrow; black squares) compared to similar spray-dried and reconstituted formulations (red circles); (g) 5 μg prime per boost on days 0/21 with a suspension of HPV16 L1 capsomeres adsorbed on alum (indicated by black arrow; black squares) compared to a single 10 μg immunization with alum-adsorbed spray-dried capsomeres coated with Al_2O_3 for 250 ALD cycles on day 0 (red triangles). Adapted from ref. 203 with permission from Springer Nature, copyright 2020.

approximately 2.3 Å per cycle was achieved (Fig. 14c), which allowed for controlling the coating thickness at the sub-nanometer level. The evaluation of ALD-coated vaccine formulations demonstrated their effectiveness in achieving delayed antigen release, robust immune responses, and enhanced thermostability. *In vivo* imaging of mice injected with ALD-coated microparticles containing infrared-labeled HPV16 L1 protein revealed that the antigen release could be tuned by varying the coating thickness. While uncoated antigen dispersed from the injection site within 1–3 weeks (Fig. 14d), particles coated with Al_2O_3 for 100 ALD cycles persisted up to 4 weeks, and those with 250–500 ALD cycles remained detectable for nearly 4 months (Fig. 14e), indicating a sustained antigen depot effect. Immunogenicity studies over a 4-month period showed that spray-dried and ALD-coated formulations elicited total and neutralizing antibody titers that were equivalent or superior to a standard alum-adsorbed two-dose immunization of the L1 protein (Fig. 14e–g). Importantly, it was found that the capsomeres were antigenically unaffected by the coating process; in fact, the Al_2O_3 layer itself acted as an effective adjuvant, eliminating the need for additional internal alum. Moreover, the storage stability at 50 °C for one month did not diminish the immune response to the ALD-coated formulations, in contrast to the degradation in the commercial liquid

vaccines under the same conditions. These findings indicate the potential of ALD technology in enabling thermostable, single-dose vaccines with tunable immune response timing and simplified logistics.

Based on this concept, Witeof *et al.* advanced the platform by formulating a trivalent HPV vaccine containing L1 capsomeres of HPV types 16, 18, and 31.[205] These were similarly spray-dried into glassy microparticles and then coated with ~50 nm of Al_2O_3 by ALD. Remarkably, even after three months of incubation at 50 °C and 70 °C, the coated vaccines retained structural integrity and elicited higher total and neutralizing antibody responses than did two-dose regimens of liquid or reconstituted spray-dried formulations. The ALD-coated particles not only demonstrated thermal and physical stability but also triggered sustained immune responses, indicating the potential of ALD to create durable and potent vaccines suitable for deployment in regions lacking reliable refrigeration infrastructure. In the most recent study, Brubaker *et al.* systematically investigated the tunable control of vaccine release and immune response kinetics using ALD. Antigen powders containing ovalbumin (OVA) were coated with Al_2O_3 layers of varying thicknesses, corresponding to 50 to 1000 ALD cycles.[206] *In vitro* dissolution studies confirmed that thicker coatings led to more prolonged antigen release, which was mirrored by a corresponding delay *in vivo* antibody responses in mice. Notably, the median time to seroconversion shifted from 2 weeks (50 ALD cycles) to as long as 36 weeks (1000 ALD cycles). Despite the delayed onset, the magnitude of antibody responses remained robust, even for delayed-release formulations. This work established a strong *in vitro–in vivo* correlation, providing a clear design framework for tailoring immune response timing through precise ALD process control.

By combining dose-sparing, delayed-release capability, and thermal stability, ALD-coated vaccine powders provide a viable path toward single-administration vaccines, especially for antigens requiring multiple exposures to achieve protective immunity. This technology holds a great potential to improve vaccination coverage, reduce logistic burdens, and facilitate rapid and equitable immunization. Most recently, the application of ALD in controlled release of pharmaceuticals has also been demonstrated for enhancing bioavailability of poorly water-soluble drugs, one of the most pressing challenges in pharmaceutical development.[223,224] This approach utilizes the ability to improve dispersibility and wettability of poorly soluble pharmaceuticals by surface engineering. This is demonstrated by a recent study by Ganapathy *et al.*,[225] who applied ALD to enhance the bioavailability fenofibrate – a BCS Class II drug with inherently low aqueous solubility.[226] In their study, ultrathin films of SiO_2 and ZnO were deposited onto fenofibrate powders using ALD in a rotary reactor operating at room temperature. The study on the effects of coating on the powder wettability, flowability, *in vitro* dissolution, and *in vivo* pharmacokinetics revealed that SiO_2-coated fenofibrate exhibited superior wettability, strongly reducing the water contact angle (Fig. 15a–c), while ZnO-coated fenofibrate improved powder flowability by reducing cohesion between particles. *In vitro* dissolution tests showed that both the ZnO- and the SiO_2-coated fenofibrate strongly improved the dissolution rate in both powder and capsule forms (Fig. 15d and e). The ALD-coated fenofibrate was dissolved completely in water containing 0.75% sodium dodecyl sulfate (SDS), compared to lower than 60% for the uncoated drug in 1 hour. Nevertheless, it was reported that the coating did not result in any improvement in solubility of fenofibrate. Furthermore, *in vivo* pharmacokinetic studies in dogs and rats demonstrated substantial increases in bioavailability of approximately twofold and in peak serum concentration of approximately threefold compared to the coated drug (Fig. 15f and g). Notably, a 28-day subacute toxicity study in rodents confirmed the safety and biocompatibility of the coatings. This case study demonstrates the versatility of ALD beyond extended- and delayed-release formulations, showcasing its utility in accelerating drug release for poorly soluble compounds. As such, ALD shows great potential as a generalizable platform to address solubility-limited bioavailability, which is a major bottleneck in the development pipeline of modern therapeutics.

It is important to discuss the mechanism of the prolonged release of pharmaceutical powders achieved by ALD coating. As mentioned above, La Zara *et al.* observed that during the dissolution, the oxide-coated budesonide particles remained intact.[199] Hence, it was suggested that the release mechanism is primarily diffusion-based, involving inward transport of the dissolution medium through sub-nanoscale pores and defects in the ALD film, followed by outward diffusion of the dissolved budesonide. Consequently, the release rate can be controlled by the coating thickness, which is translated into the number of ALD cycles. This mechanism has been adopted to explain the delayed dissolution and release of ALD-coated polymer nanofibers,[227] and holds for the ALD-coated drug-loaded ASD systems based on posaconazole (PCZ) and hydroxypropyl methylcellulose acetate succinate (HPMCAS), as schematically described in Fig. 16.[200]

Nevertheless, a recent study by Benson *et al.* provides critical insights into the drug release mechanisms of Al_2O_3-coated ASDs.[218] Using ritonavir (RTV) and polyvinylpyrrolidone/vinyl acetate copolymer (PVPVA) as the model system, ASDs were prepared by hot-melt extrusion at drug loadings of 10% and 20%, followed by Al_2O_3 coating *via* TMA/H_2O ALD at 35 °C with a controlled growth rate of 0.4 nm per cycle. The study systematically examined the effects of the coating thickness and conformality on drug release and found that in their case the defect density, rather than the thickness of the coating, is the dominant factor governing the release rate. When sufficient defects are present, coated and uncoated powders exhibit similar rapid and complete drug release regardless of the coating thickness due to the facilitated solvent penetration and faster hydration. In contrast, highly conformal coatings hinder the water ingress and delay the release. This effect is more pronounced in tablets, where compressed, coated ASD particles exhibit reduced hydration and form interconnected drug-rich domains that limit dissolution. However, this limitation can be addressed by incorporating suitable disintegrants into the tablet formulation, which enhances water penetration and disperses ASD particles more effectively. The study not only

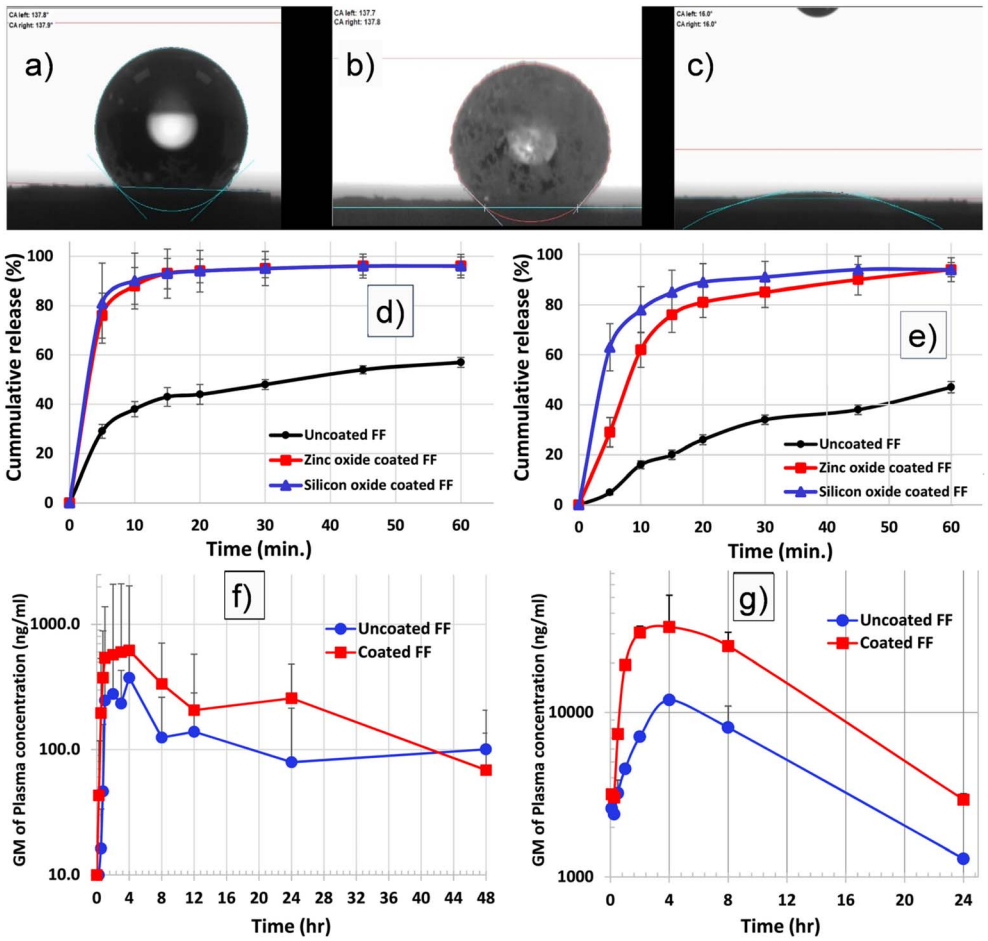

Fig. 15 Water droplets on powder bed of (a) uncoated fenofibrate, (b) ZnO-coated fenofibrate, and (c) SiO_2-coated fenofibrate. Dissolution profile of uncoated and ALD (ZnO, SiO_2)-coated fenofibrate with 0.75% sodium dodecyl sulfate (SDS) in water (d) in powder form and (e) as a capsule containing 120 mg of fenofibrate. Geometric mean (GM) plasma level-concentration profile of fenofibric acid over time after administration of SiO_2-coated and uncoated API by oral route (f) as a capsule in beagle dogs for 48 h and (g) as a powder in rats for 24 h. Adapted from ref. 225 with permission from Elsevier, copyright 2025.

demonstrates the critical role of coating structure in modulating drug release but also provides a practical formulation strategy to mitigate the release delays caused by reduced hydration kinetics.

Enhanced physical properties of pharmaceutical powders

In addition to its demonstrated roles in controlling drug release and enhancing bioavailability, ALD has also shown great potential in modifying other physical properties of

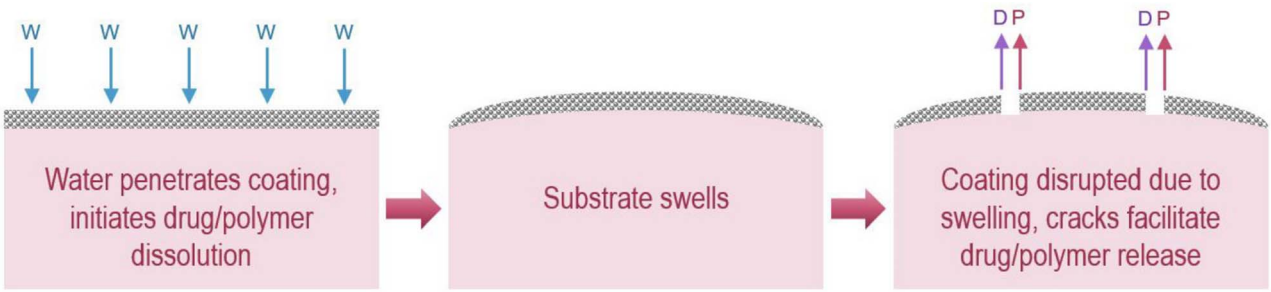

Fig. 16 Dissolution mechanism of ALC-coated ASD particles: first, water (W) penetrates through voids in the coating, initiating dissolution of the drug (D) and polymer (P). As hydration continues, the substrate swells, disrupting the coating and generating cracks. Drug and polymer can release through voids in the coating or through newly developed cracks and exposed surfaces. Reproduced from ref. 200 with permission from American Chemical Society, copyright 2023.

pharmaceutical powders. This is an equally critical aspect of drug processing and manufacturing.[212] The surface characteristics of APIs and excipients, such as flowability, wettability, and dispersibility, play a pivotal role in determining the processability, content uniformity, and overall performance of solid dosage forms. Poor flow behavior or particle agglomeration can lead to manufacturing inefficiencies, inconsistent dosing, and reduced bioavailability. By depositing conformal, nanometer-thin films on pharmaceutical particles, ALD enables precise surface engineering without altering the core material, thereby providing an effective solution to improve powder handling and processing. This section discusses the recent progress in applying ALD to tailor the surface properties to improve stability as well as processability of pharmaceutical powders.

A pioneering demonstration of the application of ALD in enhancing moisture resistance and long-term stability of hygroscopic pharmaceutical powders was reported by Hellrup *et al.*,[207] who applied Al_2O_3 ALD to coat amorphous lactose microparticles, a common excipient in pharmaceutical manufacturing.[228] To achieve uniform coating of individual particles and minimized agglomerate formation, an intermediate redispersion step was incorporated after a certain number of ALD cycles during the coating. The resulting nanoshells, accounting for up to 18 wt% of the total sample mass, were shown to be pinhole-free and conformal, without inducing any recrystallization of the amorphous lactose core. The dynamic vapor sorption analysis revealed that the moisture uptake was nearly eliminated in the samples coated with four sets of 50 or two sets of 100 ALD cycles, indicating highly effective moisture barriers. In the long-term stability studies, the uncoated amorphous lactose underwent rapid recrystallization within hours at 40 °C/75% RH, whereas the ALD-coated samples remained largely amorphous after six months, with only ~15% of particles exhibiting localized crystallization. This limited recrystallization was attributed to incomplete coating in a minority of particles, as visualized by polarized light microscopy. Additionally, dissolution tests confirmed that the Al_2O_3 shells, while relatively insoluble, gradually dissolved in biologically relevant media, indicating their potential suitability for controlled-release applications. The study demonstrates the effectiveness of ALD in delivering strong moisture protection for moisture-sensitive pharmaceutical materials.

Recent studies have explored the application of ALD in addressing the physical instability of ASDs, which are widely used to improve the solubility and oral bioavailability of poorly water-soluble drugs.[213,214] The strong tendency to crystallize over time, particularly at the surface, where molecular mobility is higher, is a critical challenge in pharmaceutical production.[229] Traditional stabilization strategies focus primarily on bulk polymer-drug interactions to inhibit crystallization,[230] but these approaches often require high polymer content, resulting in large dosage volumes and increased pill burden. A proof-of-concept study by Duong *et al.* applied ALD (or ALC – atomic layer coating) to spray-dried ASD particles composed of ezetimibe and hydroxypropyl methylcellulose acetate succinate (HPMCAS) at high drug loadings of 50% and 70% w/w.[217] Using Al_2O_3 as the coating material, which was deposited in a rotary-type ALD reactor at 35 °C, the physical performance of the ASD powders was substantially improved. Particularly, the coated particles exhibited reduced agglomeration, lower hygroscopicity, and enhanced wettability, flowability, and compressibility. Most impressively, under accelerated storage conditions (40 °C/75% RH), the uncoated ASD samples began crystallizing within days, while the ALD-coated samples showed no signs of crystallization even after two years. The coated formulations also retained consistent drug release profiles over time, in contrast to the uncoated ones, which showed substantial decreases in drug release due to crystallization-induced changes. In a subsequent study, Moseson *et al.* evaluated the general applicability of ALD across a broader spectrum of ASD formulations.[216] Multiple drug-polymer systems, differing in chemical structure, hygroscopicity, and the presence or absence of hydroxyl functional groups, were coated with Al_2O_3 or ZnO layers ranging from 5 to 25 nm in thickness. These coatings were applied to ASDs produced by both spray drying and hot-melt extrusion. Remarkably, ALD effectively delayed or completely inhibited crystallization in all formulations for up to 48 weeks even at the highly accelerated stability testing conditions. Importantly, the crystallization inhibition was observed regardless of the coating material, particle size, or whether the drug or polymer contained anchoring hydroxyl groups. This broad effect was attributed primarily to a reduction in surface molecular mobility, rather than changes in bulk properties or water sorption behavior. Moreover, ALD consistently improved micromeritic properties such as powder flowability and compressibility, supporting its dual role in both physical stabilization and manufacturability.

Beyond enhancing stability and inhibiting crystallization, ALD has emerged as a powerful tool to fine-tune various physical properties of pharmaceutical powders, such as wettability, dispersibility, flowability, and even surface charge. These are critical for efficient drug manufacturing and effective delivery. A study by Hirschberg *et al.* applied ALD of TiO_2 and investigated its influence on the flowability of various crystalline and amorphous pharmaceutical powders, including dibasic calcium phosphate dihydrate (DCPD), sorbitol (SORB), α-lactose monohydrate (LAC), microcrystalline cellulose (MCC), and croscarmellose-sodium (Na-CC).[208] After coating with 5 ALD cycles, different levels of improvement in the flowability of the powder were observed. In particular, the ALD-coated MCC exhibited a fourfold increase in flowability, while the amorphous Na-CC and the crystalline SORB showed a threefold improvement. Although both α-LAC and DCPD displayed more modest enhancements, the improvements were still statistically significant. It was found that the coating reduced the electrostatic charge generated at particle–particle and particle–container contacts, which consequently decreased the interparticle cohesion and enhanced the powder flowability. This effect was also observed for the Al_2O_3- and TiO_2-coated palbociclib and pazopanib HCl powders, as demonstrated by Gupta *et al.*[211] Namely, Kelvin probe force microscopy (KPFM) revealed a substantial reduction by approximately fourfold in the surface contact potential of the uncoated pazopanib HCl, decreasing from 2.3 V to 0.82 V and 0.52 V after coating with Al_2O_3 and

TiO_2, respectively. Similarly, the zeta-potential measurements showed a fourfold decrease in surface charge, dropping from −32.9 mV in the uncoated drug to −7.51 mV and −8.51 mV after the Al_2O_3 and TiO_2 coatings, respectively. The results demonstrate the capability of ALD to precisely tailor both the surface charge and flow behavior of pharmaceutical powders through nanoscale surface modification.

The flowability enhancement achieved by surface coating has also been demonstrated by Zhang *et al.*,[210] who employed both ALD and molecular layer deposition (MLD) to coat micronized budesonide particles with various inorganic (Al_2O_3,

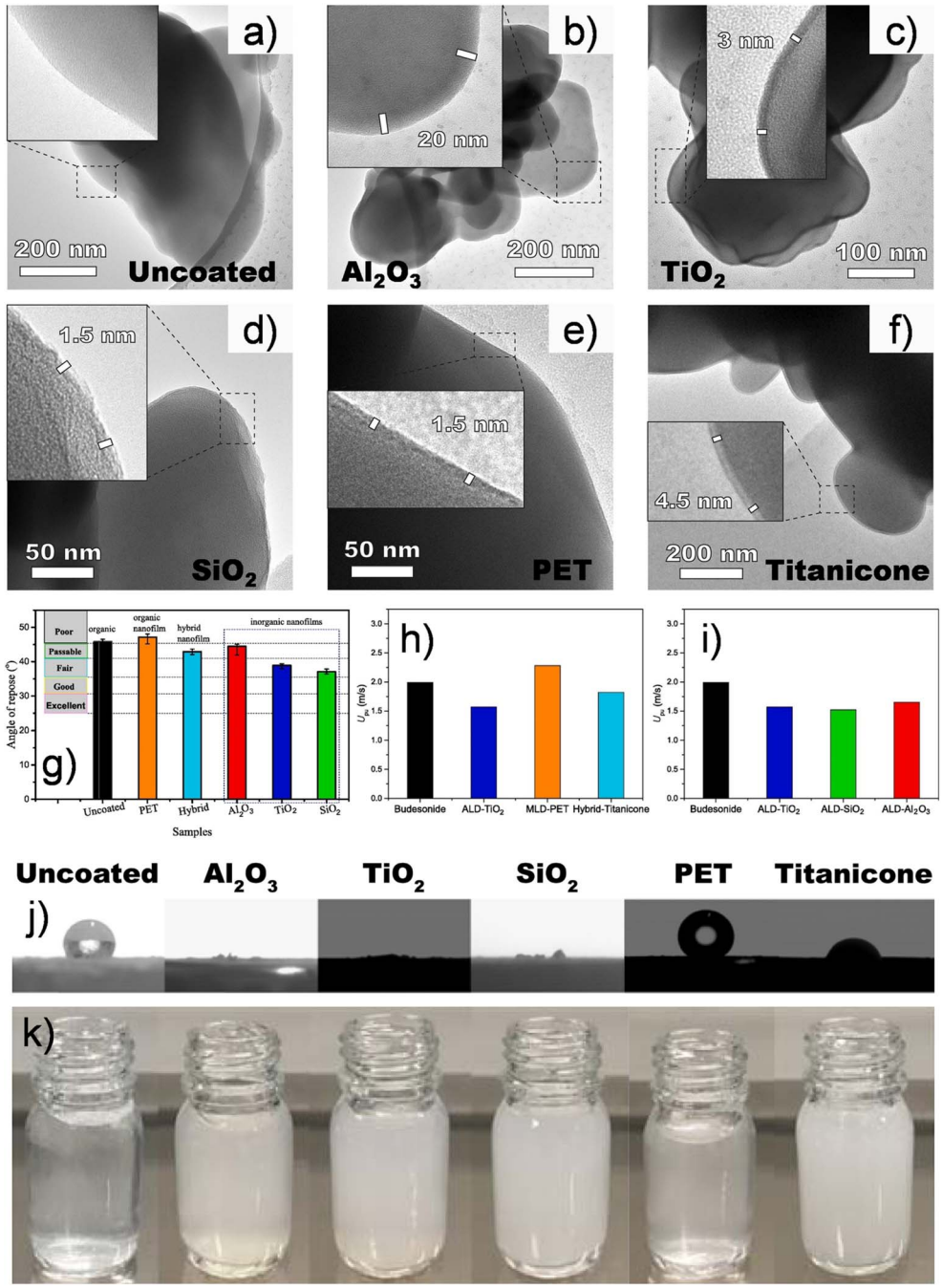

Fig. 17 TEM images budesonide particles, (a) uncoated and coated by (b) Al_2O_3, (c) TiO_2, and (d) SiO_2 films *via* ALD, (e) by poly(ethylene) terephthalate films *via* MLD, and (f) by titanicone films *via* $TiCl_4$/ethylene glycol hybrid ALD/MLD. The deposition processes of Al_2O_3, TiO_2, SiO_2, and titanicone were performed for 10 cycles, whereas that of PET was for 50 cycles. (g) Static angle of repose measured for the uncoated and coated budesonide powders: a higher static angle of repose indicates a worse flowability. (h) and (i) Minimum pick-up velocity (U_{pu}) of powders uncoated or coated *via* ALD, MLD, and hybrid coatings: a smaller U_{pu} indicates a better flowability. Adapted from ref. 210 with permission from The Authors, copyright 2023. Photographs of (j) water contact angle and (k) dispersion of the powder in water after 1 min mixing. Adapted from ref. 209 with permission from The Authors, copyright 2021.

TiO_2, and SiO_2), hybrid organic–inorganic (titanicone), and organic (polyethylene terephthalate – PET) layers (Fig. 17a–f). In their study, the flowability (or flowability) was characterized by measuring the angle of repose of the powder (static measurement) and the particles' pick-up velocity in pneumatic transport (dynamic measurement), which was determined by measuring the mass loss of the powder due to the gas flow. It was found that the inorganic and hybrid coatings significantly reduced the angle of repose (Fig. 17g) and decreased the minimum pick-up velocity (Fig. 17h and i), translating into a higher dispersibility and more efficient delivery in dry powder inhalers. In contrast, purely organic PET coatings deposited *via* MLD failed to produce similar flow improvements, indicating the critical role of surface chemistry. The origin of the enhanced flowability was investigated by means of atomic force microscopy, which revealed that the coatings by the inorganic and hybrid nanofilms significantly reduced the inter-particle forces. This consequently reduced the cohesivity between particles, promoting the flowability.

Furthermore, La Zara *et al.* demonstrated that the ALD/MLD coatings also substantially altered the wettability of budesonide powders, allowing tuning across a broad range from superhydrophilic to superhydrophobic by varying the coating materials.[209] According to the study, the uncoated budesonide showed high hydrophobicity with a stable water contact angle (WCA) of 135° over 5 min of measurements. The budesonide powders coated with the inorganic oxides (Al_2O_3, TiO_2, and SiO_2) exhibited a high hydrophilicity, with water droplets absorbing within seconds and contact angles approaching 0° rapidly regardless of the coating materials, as shown in Fig. 17j. Remarkably, the PET-coated budesonide exhibited an increased hydrophobicity, with a WCA of ~145–150°, rendering the surface superhydrophobic as the droplet remained intact over 5 min. In contrast, the titanicone-coated budesonide showed an increased hydrophilicity compared to the uncoated powder, with WCAs of ~80° and 60° for the powders after coating with 10 and 50 cycles, respectively. The tunable wettability achieved by ALD/MLD coatings enables control over the dispersibility of the powders in water, as demonstrated in Fig. 17k. The budesonide coated by ALD dispersed uniformly in water, unlike the uncoated form, which largely remained afloat due to its high hydrophobicity. Interestingly, despite its higher hydrophobicity, the PET-coated budesonide formed more stable suspensions than the uncoated powder, though much of it still floated in water after mixing. The titanicone-coated budesonide, on the other hand, produced visibly more stable suspensions, consistent with its moderate hydrophilicity observed in the WCA measurements. However, a small fraction of the titanicone-coated powder also remained on the surface, reflecting its limited wettability.

Notably, the coating significantly increased the zeta potential of the coated samples compared to the uncoated counterpart (approximately −30 mV at pH 4.8). In particular, the powders coated with Al_2O_3, TiO_2, and SiO_2 exhibited zeta potential of +52 mV (pH 5.2), +75 mV (pH 2.8), and −47 mV (pH 5.1), respectively. The titanicone coating resulted in a high zeta potential of +55 mV (pH 2.9), while the PET coating slightly increased the negative potential to −41 mV (pH 5.1). It is known that zeta potential is a key indicator of dispersion stability. A zeta potential with the magnitude of ≥30 mV is typically considered adequate for achieving good dispersion and stability.[231] Therefore, the enhanced dispersion observed for the coated powders was attributed by the increased zeta potential caused by the coating layer. These results indicate an additional benefit of ALD and MLD in enhancing the dispersion of pharmaceutical powders, which has recently been further demonstrated for diclofenac sodium (DCF) powders. This is a hydrophilic pharmaceutical that shows rapid sedimentation in water. The coating of DCF with an ultrathin layer of SiO_2 by ALD at ambient conditions (atmospheric pressure and room temperature) significantly increased the zeta potential of the powders, which effectively prevented the sedimentation and enabled a highly stable dispersion.[232]

It can be concluded that ALD provides feasible and innovative pathways in pharmaceutical powder engineering by enabling precise, nanometer-scale coatings that enhance controlled drug release and optimize powder behavior during processing. ALD coatings can act as physical barriers that modulate drug dissolution rates, protect sensitive active pharmaceutical ingredients (APIs) from environmental degradation, and extend shelf life. Moreover, ALD substantially improves powder flowability, dispersibility, and prevents agglomeration, which are the key factors in pharmaceutical manufacturing and therapies. These capabilities make ALD a promising technology for overcoming formulation challenges, achieving uniformity in drug delivery, and enabling new product designs in pharmaceutical manufacturing.

In light of the above studies, ALD has been proven to be applicable to a wide range of APIs. So far, no abnormality in release profiles or adverse biological effects on tested animals has been detected in ALD-coated API,[199,203,217,220] indicating the safety, biocompatibility, and feasibility of the technology. Generally, challenges in pharmaceutical science such as controlled release, dispersibility and flowability are addressed independently by distinct solutions. As revealed by the aforementioned studies, ALD coatings can simultaneously improve various unfavorable attributes. Furthermore, ALD itself is versatile, in which the coating process becomes possible regardless of which precursor and co-reactant are used. In other words, as long as a coating material favorable for a desired effect on pharmaceutical powder is identified, the experiment can be initiated and create proper coating layers.

In comparison to other coating techniques employed in the pharmaceutical industry, ALD offers several advantages. Not to mention obvious requirements regarding safety, which is sometimes observed to fail in solvent-based coating,[233] ALD has been demonstrated to result in promising advantages in coating quality. Initially, this technique outperforms other counterparts in terms of yielding a uniform coating layer with the capability of controlling the thickness at the sub-nanometer level. This arises from the self-limiting surface reactions of ALD,[8,9] which are totally absent in the current pharmaceutical coating techniques.[234] In addition, the applicability to various types of APIs is perceived as another challenge to traditional coating

techniques. In fact, whereas spray drying involves atomization of both APIs and coating materials and, thus, the powder must inevitably be heated up, other approaches such as hot-melt extrusion also involve melting a mixture of APIs and excipients.[235] Therefore, they are usually incompatible with thermosensitive pharmaceutical powders such as biological compounds. Meanwhile, electrostatic coating can pose safety risk to a great number of pharmaceutical powders, which have high resistivity value and, as a consequence, may accumulate charge easily.[236] By contrast, since ALD can progress at low temperatures and even at ambient conditions, and its prerequisite is only the existence of functional groups in the molecular structure, which are casual groups such as –OH and $–NH_2$,[182,237] it is expected that once proper condition is thoroughly investigated, it can be applied to a wider range of APIs. A disadvantage may be that it modifies the pharmaceutical molecules on the outside of the particle by the surface reaction, potentially leading to compounds with an undesired effect. This will require further investigation.

From the instrumentation point of view, the use of FBRs can be seen as a one-size-fit-all approach. Nevertheless, when applied to pharmaceutical powders, which have a noticeable inter-particle interaction, several limitations of FB-ALD have been identified. Initially, clumping, where the inert gas fails to disintegrate the bulk into smaller portions of particles but lifts the entire bed up in the reacting chamber, is frequently observed. This can be resolved by maintaining a flow of inert gas, by which moisture is vaporized, liquid bridge can be tackled, and the inter-particle cohesive interaction will accordingly decrease.[238] Additionally, even when fluidization is initiated, whether it sustains throughout the coating process, especially during the first several cycles, remains uncertain. The reason behind this is that the cohesive interaction among organic powder particles cannot be eliminated, so when inert gas is delivered, a channel can be formed; consequently, it tends to flow through such channels, which halts fluidization due to a reduced drag force. Moreover, agglomeration is not totally broken apart even though smooth fluidization is attainable,[239,240] thereby gas–solid contact becomes less favorable, and precursor, along with co-reactant, tend to pass on the exposed surface of clusters rather than penetrate into the contacted area among particles. Hence, it has been witnessed that consistence coating on every single particles is nearly impossible, and the coating layer may be deposited onto the entire agglomerations.[201] While this seems to be inevitable in a coating process, its impacts on further manufacture in pharmaceutical industry can be alleviated by sieving or agitation aftermath, or in-between cycles of long coating processes.[203,207,220] Moreover, to enhance fluidization, several strategies, such as strict control of particle size or using vibration, stirring and jet methods as mentioned above, should be taken into consideration.[38,58,67,68,199,201]

Most of studies on pharmaceutical coatings using FB-ALD reported mostly at the scale of 10–20 g of powder per experiment.[199,201,209,210,219,232] This is far below the minimum batch mass in manufacture, however, this may be commercially significant in the case of APIs that are prescribed at a low dose and indicated for innovative therapies, as we see in the case of single-dose vaccine.[203–205] Additionally, large-scale FB-ALD systems for powder engineering are nowadays commercially available from various providers such as Forge Nano and Applied Materials (The USA), making mass-production more feasible. Although recent advances in FB-ALD have demonstrated the feasibility of processing powders at larger scales, several challenges remain for its broader industrial implementation. These include the cost of ALD precursors, precursor usage efficiency under high carrier-gas flow, and relatively long processing times. However, it is important to note that these limitations are highly application- and process-dependent. For example, many commonly used ALD precursors, such as TMA for Al_2O_3 deposition, can be obtained at substantially reduced cost when purchased at industrial scale, and are already widely employed in pharmaceutical and catalyst applications. In addition, fluidized-bed reactors, when properly designed and operated, can achieve high precursor utilization efficiency, as demonstrated in the study of Grillo *et al.*[130] In this context, the processing time currently represents the most critical challenge, particularly for high-throughput manufacturing. Alternatively, rotary reactors or pneumatic transport reactors (Powall, The Netherlands) are ideal choices for larger scales. Numerous studies have shown successful deposition at the scale of 100 g and few kilograms of powder with excellent control of the film thickness and composition, as well as the therapeutic performance of the coating layers.[198,200,211,212,216,217]

Despite the advantages in achieving highly controllable and uniform depositions, one of the critical challenges of ALD is the use of precursors that are often chemically complex, moisture-sensitive and potentially hazardous. Many commonly used metal–organic and halide precursors (*e.g.*, TMA, DEZ, $SiCl_4$ and $TiCl_4$) can be highly flammable or corrosive, requiring strict process control, high-purity environments and efficient exhaust gas treatment to prevent negative environmental impacts. In the context of pharmaceutical applications, where the coated materials may come into direct or indirect contact with biological systems, precursor safety and the potential for residual contamination are of particular concern. Therefore, ensuring complete chemical reactions and by-product removal is crucial. To address these challenges, developing greener ALD chemistries, including precursors with lower toxicity, improved thermal stability and higher reactivity under mild conditions is highly essential. Moreover, the use of environmentally benign reactants such as water, ozone or plasma-generated species can further minimize hazardous by-products.[241,242] These ongoing efforts are expected to enhance the sustainability and biocompatibility of ALD processes, facilitating their broader adoption in pharmaceutical and biomedical applications.

Furthermore, the biological safety and long-term fate of ALD-deposited materials remain key concerns. When a coated particle is dissolved, the ceramic coating material is likely to remain present in the form of flakes with a nanoscale thickness. Nanomaterials can interact with biological membranes, proteins and cellular organelles in complex ways, and several studies have reported their potential to accumulate in tissues such as the liver, spleen, lungs, and even the central nervous

system after prolonged exposure.[243,244] The extent of accumulation and biological persistence depends strongly on particle size and shape, surface chemistry, crystallinity and dissolution rate. ALD coatings, when carefully designed, can mitigate several toxicity pathways by reducing surface reactivity, improving dispersibility and providing physical or chemical barriers against undesirable dissolution. For instance, thin ALD layers of Al_2O_3, TiO_2 and ZrO_2 have been shown to enhance chemical stability and biocompatibility.[245–247] However, these coatings may also slow down biodegradation and clearance, potentially leading to long-term persistence in the body. Therefore, there is a balance between achieving functional stability and ensuring safe elimination from biological systems. Future research should focus on designing biodegradable or bio-resorbable ALD coatings that gradually dissolve under physiological conditions, such as those based on ZnO or MgO. Moreover, systematic *in vitro* and *in vivo* studies are needed to elucidate how ALD coating thickness, composition and conformality influence cellular uptake, biodistribution and excretion pathways. Incorporating toxicological assessment into the early stages of material development will be crucial for ensuring that ALD-modified nanomaterials meet both performance and safety standards for pharmaceutical and medical use.

Conclusions and outlook

Fluidized-bed atomic layer deposition presents a robust and scalable platform for tailoring the surface properties of powder-based materials with atomic-level precision. Beyond its well-established utility in depositing conformal and ultrathin films, ALD has also emerged as a powerful method for the controlled growth of metal NPs, nanoclusters, and even single atoms on high-surface-area substrates. As reviewed in this work, FB-ALD enables precise surface and structural control over powder-based materials in two rapidly emerging fields: the synthesis of advanced Pt-based catalysts for energy applications and the nanoengineering of pharmaceutical powders for improved drug delivery and formulation performance.

In the first part of this review, we addressed the fundamental challenges associated with fluidizing nanoscale powders, particularly the tendency of cohesive powder to form agglomerates. Strategies such as mechanical vibration in combination with continuous stirring and gas jets were discussed as practical methods to enhance powder fluidization. These integrations are critical for achieving uniform coating in FBR systems, which depends on ensuring maximum surface exposure during ALD processing.

The second part of the review focused on the synthesis and modification of Pt-based catalysts using FB-ALD. Key approaches for optimizing catalyst performance were highlighted, including surface pretreatment for improved nucleation, control of particle size distribution through ALD cycle tuning as well as temperature, and compositional engineering for alloy and core–shell structures. ALD also allows for the deposition of protective overlayers to enhance catalyst durability under harsh operating conditions. These capabilities are particularly relevant for applications in fuel cells and chemical processes, where stability, activity, and efficient material usage are critical.

The final part examined recent applications of ALD to pharmaceutical powders. The technique has demonstrated considerable potential in enhancing the powder flowability, dispersibility, and wettability, which are essential for formulation and manufacturing. Moreover, ALD coatings have enabled the design of controlled-release formulations, moisture-resistant amorphous drugs, and thermostable vaccines. In particular, ALD-based nanoencapsulation strategies have allowed for single-dose injectable vaccines by enabling delayed antigen release over extended timeframes, while also improving storage stability under elevated temperatures.

FB-ALD provides a unique combination of precision, scalability, and versatility for the surface modification of powders across a broad range of applications. As the materials and manufacturing challenges grow increasingly complex, this technology is expected to play an integral role in the design and production of next-generation catalysts, functional materials, and pharmaceuticals. Looking forward, the future developments in FB-ALD are likely to focus on four key areas: (1) improving reactor design and process control to handle ultrafine and thermally sensitive powders, (2) developing environmentally benign and cost-effective precursors for industrial-scale coating, (3) translation of batch-wise FB-ALD processes to industrial continuous powder ALD,[248] and (4) integrating ALD with other manufacturing platforms such as spray drying, additive manufacturing, and continuous flow synthesis. Further expansion of ALD into biologics, nanocarriers, and hybrid drug-delivery systems is of great interest, particularly with the continued advancement of low-temperature ALD processes.

Conflicts of interest

J. R. van Ommen has a financial interest in Powall.

Data availability

No primary research results, software or code have been included and no new data were generated or analysed as part of this review.

Acknowledgements

This work is funded by Phenikaa Innovation Foundation, under the grant number ĐMST.2022.03.

Notes and references

1 Y. Hu, J. Lu and H. Feng, *RSC Adv.*, 2021, **11**, 11918–11942.
2 T. K. Kim, M. N. Lee, S. H. Lee, Y. C. Park, C. K. Jung and J.-H. Boo, *Thin Solid Films*, 2005, **475**, 171–177.
3 M. Lee, W. Ahmad, D. W. Kim, K. M. Kwon, H. Y. Kwon, H.-B. Jang, S.-W. Noh, D.-H. Kim, S. J. A. Zaidi, H. Park, H. C. Lee, M. Abdul Basit and T. J. Park, *Chem. Mater.*, 2022, **34**, 3539–3587.

4 J. R. van Ommen and A. Goulas, *Mater. Today Chem.*, 2019, **14**, 100183.
5 D. M. King, X. Liang and A. W. Weimer, *Powder Technol.*, 2012, **221**, 13–25.
6 Z. Li, J. Xiang, X. Liu, X. Li, L. Li, B. Shan and R. Chen, *Int. J. Extreme Manuf.*, 2022, **4**, 025101.
7 K. Cao, J. Cai, B. Shan and R. Chen, *Sci. Bull.*, 2020, **65**, 678–688.
8 H. Van Bui, F. Grillo and J. R. Van Ommen, *Chem. Commun.*, 2017, **53**, 45–71.
9 S. M. George, *Chem. Rev.*, 2010, **110**, 111–131.
10 R. W. Johnson, A. Hultqvist and S. F. Bent, *Mater. Today*, 2014, **17**, 236–246.
11 M. Leskelä and M. Ritala, *Thin Solid Films*, 2002, **409**, 138–146.
12 V. Pore, T. Hatanpää, M. Ritala and M. Leskelä, *J. Am. Chem. Soc.*, 2009, **131**, 3478–3480.
13 J. Zhang, Z. Yu, Z. Gao, H. Ge, S. Zhao, C. Chen, S. Chen, X. Tong, M. Wang, Z. Zheng and Y. Qin, *Angew. Chem., Int. Ed.*, 2017, **56**, 816–820.
14 J. D. Ferguson, A. W. Weimer and S. M. George, *Thin Solid Films*, 2002, **413**, 16–25.
15 J. Lu, *Acc. Mater. Res.*, 2022, **3**, 358–368.
16 J. Lu, J. W. Elam and P. C. Stair, *Surf. Sci. Rep.*, 2016, **71**, 410–472.
17 B. J. O'Neill, D. H. K. Jackson, J. Lee, C. Canlas, P. C. Stair, C. L. Marshall, J. W. Elam, T. F. Kuech, J. A. Dumesic and G. W. Huber, *ACS Catal.*, 2015, **5**, 1804–1825.
18 L. Zhang, M. N. Banis and X. Sun, *Natl. Sci. Rev.*, 2018, **5**, 628–630.
19 X. Wang, R. Chen and S. Sun, *Int. J. Extreme Manuf.*, 2023, **5**, 043001.
20 J. A. Singh, N. Yang and S. F. Bent, *Annu. Rev. Chem. Biomol. Eng.*, 2017, **8**, 41–62.
21 Z. Gao and Y. Qin, *Acc. Chem. Res.*, 2017, **50**, 2309–2316.
22 B. Gupta, Md. A. Hossain, A. Riaz, A. Sharma, D. Zhang, H. H. Tan, C. Jagadish, K. Catchpole, B. Hoex and S. Karuturi, *Adv. Funct. Mater.*, 2022, **32**, 2109105.
23 M. Atwa, X. Li, Z. Wang, S. Dull, S. Xu, X. Tong, R. Tang, H. Nishihara, F. Prinz and V. Birss, *Mater. Horiz.*, 2021, **8**, 2451–2462.
24 C. Liu, C.-C. Wang, C.-C. Kei, Y.-C. Hsueh and T.-P. Perng, *Small*, 2009, **5**, 1535–1538.
25 C.-C. Chao, M. Motoyama and F. B. Prinz, *Adv. Energy Mater.*, 2012, **2**, 651–654.
26 G. Yan, G. Huang, J. Shi, Y. Ouyang, X. Zuo, Z. Bao and Y. Mei, *Adv. Mater. Interfaces*, 2025, **12**, e00140.
27 D. Longrie, D. Deduytsche and C. Detavernier, *J. Vac. Sci. Technol., A*, 2013, **32**, 010802.
28 S. Haukka, E.-L. Lakomaa and T. Suntola, *Thin Solid Films*, 1993, **225**, 280–283.
29 J. W. Elam, M. D. Groner and S. M. George, *Rev. Sci. Instrum.*, 2002, **73**, 2981–2987.
30 D. M. King, J. A. Spencer, X. Liang, L. F. Hakim and A. W. Weimer, *Surf. Coat. Technol.*, 2007, **201**, 9163–9171.
31 D. M. King, X. Liang, Y. Zhou, C. S. Carney, L. F. Hakim, P. Li and A. W. Weimer, *Powder Technol.*, 2008, **183**, 356–363.
32 J. A. McCormick, B. L. Cloutier, A. W. Weimer and S. M. George, *J. Vac. Sci. Technol., A*, 2007, **25**, 67–74.
33 D. Longrie, D. Deduytsche, J. Haemers, K. Driesen and C. Detavernier, *Surf. Coat. Technol.*, 2012, **213**, 183–191.
34 Y. S. Jung, A. S. Cavanagh, A. C. Dillon, M. D. Groner, S. M. George and S.-H. Lee, *J. Electrochem. Soc.*, 2009, **157**, A75.
35 J. R. van Ommen, D. Kooijman, M. de Niet, M. Talebi and A. Goulas, *J. Vac. Sci. Technol., A*, 2015, **33**, 021513.
36 A. W. Weimer, *J. Nanopart. Res.*, 2019, **21**, 9.
37 A. W. Weimer, *Powder Technol.*, 2023, **418**, 118279.
38 R. Beetstra, U. Lafont, J. Nijenhuis, E. M. Kelder and J. R. van Ommen, *Chem. Vap. Deposition*, 2009, **15**, 227–233.
39 F. Grillo, M. T. Kreutzer and J. R. van Ommen, *Chem. Eng. J.*, 2015, **268**, 384–398.
40 J. R. van Ommen, J. M. Valverde and R. Pfeffer, *J. Nanopart. Res.*, 2012, **14**, 737.
41 D. Geldart, *Powder Technol.*, 1973, **7**, 285–292.
42 X. Zhu, Q. Zhang, Y. Wang and F. Wei, *Chin. J. Chem. Eng.*, 2016, **24**, 9–22.
43 A. Bahramian, *J. Nanopart. Res.*, 2019, **21**, 196.
44 L. de Martín, W. G. Bouwman and J. R. van Ommen, *Langmuir*, 2014, **30**, 12696–12702.
45 L. de Martín, J. Sánchez-Prieto, F. Hernández-Jiménez and J. R. van Ommen, *J. Nanopart. Res.*, 2013, **16**, 2183.
46 H. Liu and S. Wang, *Powder Technol.*, 2021, **388**, 122–128.
47 S. Wang and H. Liu, *Ind. Eng. Chem. Res.*, 2021, **60**, 753–761.
48 A. Bahramian and M. Olazar, *Powder Technol.*, 2021, **386**, 491–504.
49 W. Yao, G. Guangsheng, W. Fei and W. Jun, *Powder Technol.*, 2002, **124**, 152–159.
50 A. Fabre, S. Salameh, M. T. Kreutzer and J. R. van Ommen, *Powder Technol.*, 2017, **312**, 347–353.
51 M. Tahmasebpoor, R. Ghasemi Seif Abadi, Y. Rahimvandi Noupoor and P. Badamchizadeh, *Ind. Eng. Chem. Res.*, 2016, **55**, 12939–12948.
52 A. A. Esmailpour, N. Mostoufi and R. Zarghami, *Ind. Eng. Chem. Res.*, 2017, **56**, 13955–13969.
53 C. Zhu, Q. Yu, R. N. Dave and R. Pfeffer, *AIChE J.*, 2005, **51**, 426–439.
54 Q. Guo, Y. Li, M. Wang, W. Shen and C. Yang, *Chem. Eng. Technol.*, 2006, **29**, 78–86.
55 C. Mogre, A. U. Thakurdesai, J. R. van Ommen and S. Salameh, *Powder Technol.*, 2017, **316**, 441–445.
56 A. Bahramian and J. R. Grace, *Powder Technol.*, 2017, **310**, 46–59.
57 J. Gómez-Hernández, S. Sánchez-Delgado, E. Wagner, R. F. Mudde and J. R. van Ommen, *Powder Technol.*, 2017, **316**, 446–454.
58 H. Wang, T. Zhou, J.-S. Yang, J.-J. Wang, H. Kage and Y. Mawatari, *Chem. Eng. Technol.*, 2010, **33**, 388–394.
59 H. Hoorijani, R. Zarghami, K. Nosrati and N. Mostoufi, *Chem. Eng. Res. Des.*, 2021, **174**, 486–497.

60 K. Wu, R. Kamphorst, A. Bakker, J. Ford, E. C. Wagner, O. Ochkin-Koenig, M. Franck, D. Weis, G. M. H. Meesters and J. R. van Ommen, *Chem. Eng. Sci.*, 2024, **294**, 120069.
61 R. Kamphorst, K. Wu, M. van Baarlen, G. M. H. Meesters and J. R. van Ommen, *Chem. Eng. Sci.*, 2024, **291**, 119911.
62 C. Zhu, G. Liu, Q. Yu, R. Pfeffer, R. N. Dave and C. H. Nam, *Powder Technol.*, 2004, **141**, 119–123.
63 Q. Yu, R. N. Dave, C. Zhu, J. A. Quevedo and R. Pfeffer, *AIChE J.*, 2005, **51**, 1971–1979.
64 D. Lepek, J. M. Valverde, R. Pfeffer and R. N. Dave, *AIChE J.*, 2010, **56**, 54–65.
65 S. S. Ali and M. Asif, *Powder Technol.*, 2017, **310**, 234–240.
66 V. Martín, M. J. Cocero and S. Rodríguez-Rojo, *Powder Technol.*, 2017, **318**, 242–247.
67 Z. Zhao, D. Liu, J. Ma and X. Chen, *Chem. Eng. J.*, 2020, **388**, 124213.
68 L. Zhang, D. Liu, X. Wu, W. Zhang and H. Feng, *Powder Technol.*, 2023, **430**, 118996.
69 L. de Martín and J. R. van Ommen, *J. Nanopart. Res.*, 2013, **15**, 2055.
70 D. Liu, B. G. M. van Wachem, R. F. Mudde, X. Chen and J. R. van Ommen, *Powder Technol.*, 2016, **304**, 198–207.
71 D. Liu, B. G. M. van Wachem, R. F. Mudde, X. Chen and J. R. van Ommen, *AIChE J.*, 2016, **62**, 2259–2270.
72 A. Bahramian and M. Olazar, *Chem. Eng. Res. Des.*, 2021, **176**, 34–48.
73 S. Bhoi, S. R. Kolan, A. Bück and E. Tsotsas, *Powder Technol.*, 2024, **433**, 119271.
74 Y. Wu, D. Liu, B. G. M. van Wachem and J. R. van Ommen, *Ind. Eng. Chem. Res.*, 2024, **63**, 7453–7464.
75 K. M. Kellogg, P. Liu and C. M. Hrenya, *Chem. Eng. Sci.*, 2019, **199**, 249–257.
76 F. Grillo, M. T. Kreutzer and J. R. van Ommen, *Chem. Eng. J.*, 2015, **268**, 384–398.
77 J. Lu, J. W. Elam and P. C. Stair, *Acc. Chem. Res.*, 2013, **46**, 1806–1815.
78 B. Zhang and Y. Qin, *ACS Catal.*, 2018, **8**, 10064–10081.
79 J. Fonseca and J. Lu, *ACS Catal.*, 2021, **11**, 7018–7059.
80 S. Sun, G. Zhang, N. Gauquelin, N. Chen, J. Zhou, S. Yang, W. Chen, X. Meng, D. Geng, M. N. Banis, R. Li, S. Ye, S. Knights, G. A. Botton, T.-K. Sham and X. Sun, *Sci. Rep.*, 2013, **3**, 1775.
81 N. Cheng, S. Stambula, D. Wang, M. N. Banis, J. Liu, A. Riese, B. Xiao, R. Li, T.-K. Sham, L.-M. Liu, G. A. Botton and X. Sun, *Nat. Commun.*, 2016, **7**, 13638.
82 S. Fang, X. Zhu, X. Liu, J. Gu, W. Liu, D. Wang, W. Zhang, Y. Lin, J. Lu, S. Wei, Y. Li and T. Yao, *Nat. Commun.*, 2020, **11**, 1029.
83 H. Wang, C. Wang, H. Yan, H. Yi and J. Lu, *J. Catal.*, 2015, **324**, 59–68.
84 M. J. Weber, A. J. M. Mackus, M. A. Verheijen, C. van der Marel and W. M. M. Kessels, *Chem. Mater.*, 2012, **24**, 2973–2977.
85 I. J. Hsu, Y. C. Kimmel, X. Jiang, B. G. Willis and J. G. Chen, *Chem. Commun.*, 2012, **48**, 1063–1065.
86 K. Cao, Q. Zhu, B. Shan and R. Chen, *Sci. Rep.*, 2015, **5**, 8470.
87 W.-J. Lee, S. Bera, H.-J. Woo, W. Hong, J.-Y. Park, S.-J. Oh and S.-H. Kwon, *Chem. Eng. J.*, 2022, **442**, 136123.
88 R. Zhao, X. Du, K. Cao, M. Gong, Y. Li, J. Ai, R. Ye, R. Chen and B. Shan, *Int. J. Hydrogen Energy*, 2023, **48**, 28780–28791.
89 C. Huang, H. Liu, Y. Tang, Q. Lu, S. Chu, X. Liu, B. Shan and R. Chen, *Appl. Catal., B*, 2023, **320**, 121986.
90 C. de Paula, N. E. Richey, L. Zeng and S. F. Bent, *Chem. Mater.*, 2020, **32**, 315–325.
91 J. J. Pyeon, C. J. Cho, S.-H. Baek, C.-Y. Kang, J.-S. Kim, D. S. Jeong and S. K. Kim, *Nanotechnology*, 2015, **26**, 304003.
92 H.-B.-R. Lee and S. F. Bent, *Chem. Mater.*, 2012, **24**, 279–286.
93 M.-L. Shi, J. Xu, Y.-W. Dai, Q. Cao, L. Chen, Q.-Q. Sun, P. Zhou, S.-J. Ding and D. W. Zhang, *Vacuum*, 2017, **140**, 139–143.
94 Y. Hwang, B.-M. Nguyen and S. A. Dayeh, *Appl. Phys. Lett.*, 2013, **103**, 263115.
95 C. de Paula, N. E. Richey, L. Zeng and S. F. Bent, *Chem. Mater.*, 2020, **32**, 315–325.
96 J. J. Pyeon, C. J. Cho, S.-H. Baek, C.-Y. Kang, J.-S. Kim, D. S. Jeong and S. K. Kim, *Nanotechnology*, 2015, **26**, 304003.
97 A. A. Dameron, S. Pylypenko, J. B. Bult, K. C. Neyerlin, C. Engtrakul, C. Bochert, G. J. Leong, S. L. Frisco, L. Simpson, H. N. Dinh and B. Pivovar, *Appl. Surf. Sci.*, 2012, **258**, 5212–5221.
98 E. Antolini, *Appl. Catal., B*, 2009, **88**, 1–24.
99 W.-J. Lee, S. Bera, C. M. Kim, E.-K. Koh, W.-P. Hong, S.-J. Oh, E. Cho and S.-H. Kwon, *NPG Asia Mater.*, 2020, **12**, 1–13.
100 W.-J. Lee and S.-H. Kwon, *Part. Part. Syst. Charact.*, 2023, **40**, 2200158.
101 W.-J. Lee, S. Bera, H.-C. Shin, W.-P. Hong, S.-J. Oh, Z. Wan and S.-H. Kwon, *Adv. Mater. Interfaces*, 2019, **6**, 1901210.
102 F. Pescher, J. Stiegeler, P. A. Heizmann, C. Klose, S. Vierrath and M. Breitwieser, *RSC Adv.*, 2024, **14**, 32358–32369.
103 A. M. Lubers, A. W. Drake, D. J. Ludlow and A. W. Weimer, *Powder Technol.*, 2016, **296**, 72–78.
104 K.-H. T. Dinh, H. T. T. Ta, N. L. Nguyen, V. T. Le, V. H. Nguyen and H. Van Bui, *Chem. Mater.*, 2023, **35**, 2248–2280.
105 H. Van Bui, F. Grillo, S. Sharath Kulkarni, R. Bevaart, N. V. Thang, B. van der Linden, J. A. Moulijn, M. Makkee, M. T. Kreutzer and J. R. van Ommen, *Nanoscale*, 2017, **9**, 10802–10810.
106 F. Grillo, H. Van Bui, J. A. Moulijn, M. T. Kreutzer and J. R. van Ommen, *J. Phys. Chem. Lett.*, 2017, **8**, 975–983.
107 L.-A. T. Le, H. T. T. Ta, H. V. Bui and N. L. Nguyen, *J. Phys. Chem. C*, 2025, **129**, 705–714.
108 E. Antolini, *Appl. Catal., B*, 2016, **181**, 298–313.
109 T. Aaltonen, A. Rahtu, M. Ritala and M. Leskelä, *Electrochem. Solid-State Lett.*, 2003, **6**, C130.
110 W. M. M. Kessels, H. C. M. Knoops, S. a. F. Dielissen, A. J. M. Mackus and M. C. M. van de Sanden, *Appl. Phys. Lett.*, 2009, **95**, 013114.
111 A. J. M. Mackus, M. A. Verheijen, N. Leick, A. A. Bol and W. M. M. Kessels, *Chem. Mater.*, 2013, **25**, 1905–1911.
112 T. Aaltonen, M. Ritala, T. Sajavaara, J. Keinonen and M. Leskelä, *Chem. Mater.*, 2003, **15**, 1924–1928.

113 J. Dendooven, R. K. Ramachandran, K. Devloo-Casier, G. Rampelberg, M. Filez, H. Poelman, G. B. Marin, E. Fonda and C. Detavernier, *J. Phys. Chem. C*, 2013, **117**, 20557–20561.
114 H.-B.-R. Lee and S. F. Bent, *Chem. Mater.*, 2015, **27**, 6802–6809.
115 T. D. Gould, A. M. Lubers, A. R. Corpuz, A. W. Weimer, J. L. Falconer and J. W. Medlin, *ACS Catal.*, 2015, **5**, 1344–1352.
116 W. Setthapun, W. D. Williams, S. M. Kim, H. Feng, J. W. Elam, F. A. Rabuffetti, K. R. Poeppelmeier, P. C. Stair, E. A. Stach, F. H. Ribeiro, J. T. Miller and C. L. Marshall, *J. Phys. Chem. C*, 2010, **114**, 9758–9771.
117 M. Nemiwal, T. C. Zhang and D. Kumar, *Int. J. Hydrogen Energy*, 2021, **46**, 21401–21418.
118 P. Yang, X. Yang, W. Liu, R. Guo and Z. Yao, *Green Energy Environ.*, 2023, **8**, 1265–1278.
119 C. Tan, X. Huang and H. Zhang, *Mater. Today*, 2013, **16**, 29–36.
120 J. Liu, Q. Ma, Z. Huang, G. Liu and H. Zhang, *Adv. Mater.*, 2019, **31**, 1800696.
121 T. Lagarteira, S. Delgado, C. Fernandes, C. Azenha, C. Mateos-Pedrero and A. Mendes, *Int. J. Hydrogen Energy*, 2020, **45**, 20594–20604.
122 J. I. Choi, H. S. Kim, Y.-J. Sohn, S.-D. Yim, F. M. Alamgir and S. S. Jang, *ACS Appl. Nano Mater.*, 2021, **4**, 1067–1075.
123 N. Seselj, C. Engelbrekt and J. Zhang, *Sci. Bull.*, 2015, **60**, 864–876.
124 L. Zhao, Z.-B. Wang, J.-L. Li, J.-J. Zhang, X.-L. Sui and L.-M. Zhang, *J. Mater. Chem. A*, 2015, **3**, 5313–5320.
125 E. Antolini, *Appl. Catal., B*, 2012, **123–124**, 52–68.
126 H. Yan, Y. Lin, H. Wu, W. Zhang, Z. Sun, H. Cheng, W. Liu, C. Wang, J. Li, X. Huang, T. Yao, J. Yang, S. Wei and J. Lu, *Nat. Commun.*, 2017, **8**, 1070.
127 C.-T. Hsieh, W.-Y. Chen, D.-Y. Tzou, A. K. Roy and H.-T. Hsiao, *Int. J. Hydrogen Energy*, 2012, **37**, 17837–17843.
128 C.-T. Hsieh, Y.-Y. Liu, D.-Y. Tzou and W.-Y. Chen, *J. Phys. Chem. C*, 2012, **116**, 26735–26743.
129 A. J. M. Mackus, D. Garcia-Alonso, H. C. M. Knoops, A. A. Bol and W. M. M. Kessels, *Chem. Mater.*, 2013, **25**, 1769–1774.
130 F. Grillo, H. Van Bui, D. La Zara, A. A. I. Aarnink, A. Y. Kovalgin, P. Kooyman, M. T. Kreutzer and J. R. van Ommen, *Small*, 2018, **14**, 1800765.
131 H. V. Bui, A. P. Nguyen, M. D. Dang, T. D. Dinh, P. J. Kooyman and J. R. V. Ommen, *Chem. Commun.*, 2024, **60**, 14045–14048.
132 C. T. Campbell, *Surf. Sci. Rep.*, 1997, **27**, 1–111.
133 J. Lu, K.-B. Low, Y. Lei, J. A. Libera, A. Nicholls, P. C. Stair and J. W. Elam, *Nat. Commun.*, 2014, **5**, 3264.
134 Y. Lei, B. Liu, J. Lu, R. J. Lobo-Lapidus, T. Wu, H. Feng, X. Xia, A. U. Mane, J. A. Libera, J. P. Greeley, J. T. Miller and J. W. Elam, *Chem. Mater.*, 2012, **24**, 3525–3533.
135 K. Cao, J. Cai, X. Liu and R. Chen, *J. Vac. Sci. Technol., A*, 2018, **36**, 010801.
136 M. J. Weber, M. A. Verheijen, A. A. Bol and W. M. M. Kessels, *Nanotechnology*, 2015, **26**, 094002.
137 H. Wang, C. Wang, H. Yan, H. Yi and J. Lu, *J. Catal.*, 2015, **324**, 59–68.
138 X. Jiang and S. F. Bent, *J. Phys. Chem. C*, 2009, **113**, 17613–17625.
139 R. Chen and S. F. Bent, *Adv. Mater.*, 2006, **18**, 1086–1090.
140 Z.-P. Wu, D. T. Caracciolo, Y. Maswadeh, J. Wen, Z. Kong, S. Shan, J. A. Vargas, S. Yan, E. Hopkins, K. Park, A. Sharma, Y. Ren, V. Petkov, L. Wang and C.-J. Zhong, *Nat. Commun.*, 2021, **12**, 859.
141 K. Kodama, T. Nagai, A. Kuwaki, R. Jinnouchi and Y. Morimoto, *Nat. Nanotechnol.*, 2021, **16**, 140–147.
142 C. Zhan, Y. Xu, L. Bu, H. Zhu, Y. Feng, T. Yang, Y. Zhang, Z. Yang, B. Huang, Q. Shao and X. Huang, *Nat. Commun.*, 2021, **12**, 6261.
143 S. Zhu, X. Qin, F. Xiao, S. Yang, Y. Xu, Z. Tan, J. Li, J. Yan, Q. Chen, M. Chen and M. Shao, *Nat. Catal.*, 2021, **4**, 711–718.
144 D. Wu, X. Shen, Y. Pan, L. Yao and Z. Peng, *ChemNanoMat*, 2020, **6**, 32–41.
145 H. A. Gasteiger, S. S. Kocha, B. Sompalli and F. T. Wagner, *Appl. Catal., B*, 2005, **56**, 9–35.
146 T. Đukić, L. Pavko, P. Jovanovič, N. Maselj, M. Gatalo and N. Hodnik, *Chem. Commun.*, 2022, **58**, 13832–13854.
147 Z. W. Chen, J. Li, P. Ou, J. E. Huang, Z. Wen, L. Chen, X. Yao, G. Cai, C. C. Yang, C. V. Singh and Q. Jiang, *Nat. Commun.*, 2024, **15**, 359.
148 C. Kim, F. Dionigi, V. Beermann, X. Wang, T. Möller and P. Strasser, *Adv. Mater.*, 2019, **31**, 1805617.
149 B.-A. Lu, T. Sheng, N. Tian, Z.-C. Zhang, C. Xiao, Z.-M. Cao, H.-B. Ma, Z.-Y. Zhou and S.-G. Sun, *Nano Energy*, 2017, **33**, 65–71.
150 P. Hernandez-Fernandez, F. Masini, D. N. McCarthy, C. E. Strebel, D. Friebel, D. Deiana, P. Malacrida, A. Nierhoff, A. Bodin, A. M. Wise, J. H. Nielsen, T. W. Hansen, A. Nilsson, I. E. L. Stephens and I. Chorkendorff, *Nat. Chem.*, 2014, **6**, 732–738.
151 A. Velázquez-Palenzuela, F. Masini, A. F. Pedersen, M. Escudero-Escribano, D. Deiana, P. Malacrida, T. W. Hansen, D. Friebel, A. Nilsson, I. E. L. Stephens and I. Chorkendorff, *J. Catal.*, 2015, **328**, 297–307.
152 Y. Song, Y. Ma, Y. Wang, J. Di and Y. Tu, *Electrochim. Acta*, 2010, **55**, 4909–4914.
153 L. Zhao, Y. Guo, C. Fu, L. Luo, G. Wei, S. Shen and J. Zhang, *Chin. J. Catal.*, 2021, **42**, 2068–2077.
154 C. Wang, N. M. Markovic and V. R. Stamenkovic, *ACS Catal.*, 2012, **2**, 891–898.
155 J. Lu, K.-B. Low, Y. Lei, J. A. Libera, A. Nicholls, P. C. Stair and J. W. Elam, *Nat. Commun.*, 2014, **5**, 3264.
156 L. Zhang, R. Si, H. Liu, N. Chen, Q. Wang, K. Adair, Z. Wang, J. Chen, Z. Song, J. Li, M. N. Banis, R. Li, T.-K. Sham, M. Gu, L.-M. Liu, G. A. Botton and X. Sun, *Nat. Commun.*, 2019, **10**, 4936.
157 J. Lu, J. W. Elam and P. C. Stair, *Acc. Chem. Res.*, 2013, **46**, 1806–1815.
158 B. Zhang and Y. Qin, *ACS Catal.*, 2018, **8**, 10064–10081.
159 H. Song, B. Wang, J. Shin, Y.-K. Park, T. Kyun Kim, H. Paik, H. Seo, J. Lim, D. Kwon, K. Lee, Y. Sin Kim, D. Hoon Shin

and C. Seong Hwang, *J. Mater. Chem. C*, 2024, **12**, 2714–2722.
160 Z.-X. Zhang, F.-B. Ren, C.-H. Hsu, X.-Y. Zhang, P. Gao, W.-Y. Wu, D.-S. Wuu, L. Jiang, Y. Qiu, F.-M. Lai, S.-Y. Lien and W.-Z. Zhu, *J. Alloys Compd.*, 2024, **970**, 172488.
161 A. Hultqvist, M. Edoff and T. Törndahl, *Prog. Photovoltaics Res. Appl.*, 2011, **19**, 478–481.
162 A. Kumar, M. Devi, S. Tomer, M. Dutta and P. Pathi, Vandana, *Surf. Interfaces*, 2024, **47**, 104127.
163 M. Li, S. Fu, S. Saedy, A. Rajendrakumar, F. D. Tichelaar, R. Kortlever and J. R. van Ommen, *ChemCatChem*, 2022, **14**, e202200949.
164 Y. Gao, H. Liu, X. Wang, X. Liu, B. Shan and R. Chen, *Small*, 2024, **20**, 2405748.
165 P. Forzatti and L. Lietti, *Catal. Today*, 1999, **52**, 165–181.
166 C. H. Bartholomew, *Appl. Catal., A*, 2001, **212**, 17–60.
167 A. J. Martín, S. Mitchell, C. Mondelli, S. Jaydev and J. Pérez-Ramírez, *Nat. Catal.*, 2022, **5**, 854–866.
168 M. D. Argyle and C. H. Bartholomew, *Catalysts*, 2015, **5**, 145–269.
169 Z. Wu, B. Yang, S. Miao, W. Liu, J. Xie, S. Lee, M. J. Pellin, D. Xiao, D. Su and D. Ma, *ACS Catal.*, 2019, **9**, 2693–2700.
170 R. Zhao, K. Cao, R. Ye, Y. Tang, C. Du, F. Liu, Y. Zhao, R. Chen and B. Shan, *Chem. Eng. J.*, 2024, **491**, 151966.
171 I. Lee, Q. Zhang, J. Ge, Y. Yin and F. Zaera, *Nano Res.*, 2011, **4**, 115–123.
172 Q. Zhang, I. Lee, J. B. Joo, F. Zaera and Y. Yin, *Acc. Chem. Res.*, 2013, **46**, 1816–1824.
173 J. Huo, J.-P. Tessonnier and B. H. Shanks, *ACS Catal.*, 2021, **11**, 5248–5270.
174 D. Ding, M. Liu, Z. Liu, X. Li, K. Blinn, X. Zhu and M. Liu, *Adv. Energy Mater.*, 2013, **3**, 1149–1154.
175 R. J. O'Toole, C. J. Bartel, M. U. Kodas, A. J. Horrell, S. Ricote, N. P. Sullivan, C. J. Gump, C. B. Musgrave and A. W. Weimer, *J. Am. Ceram. Soc.*, 2019, **102**, 2283–2293.
176 J. Li, J. Wu, M. Wang, D. Wen, X. Liu, B. Shan and R. Chen, *ACS Appl. Mater. Interfaces*, 2025, **17**, 3205–3213.
177 J. W. Kim, D. H. Kim, D. Y. Oh, H. Lee, J. H. Kim, J. H. Lee and Y. S. Jung, *J. Power Sources*, 2015, **274**, 1254–1262.
178 D. Wang, J. Yang, J. Liu, X. Li, R. Li, M. Cai, T.-K. Sham and X. Sun, *J. Mater. Chem. A*, 2014, **2**, 2306–2312.
179 A. Shapira, O. Tiurin, N. Solomatin, M. Auinat, A. Meitav and Y. Ein-Eli, *ACS Appl. Energy Mater.*, 2018, **1**, 6809–6823.
180 E. Azaceta, S. García, O. Leonet, M. Beltrán, I. Gómez, A. Chuvilin, A. R. Mainar, J. A. Blazquez and M. Knez, *Mater. Today Energy*, 2020, **18**, 100567.
181 W. W. McNeary, S. F. Zaccarine, A. Lai, A. E. Linico, S. Pylypenko and A. W. Weimer, *Appl. Catal., B*, 2019, **254**, 587–593.
182 R. L. Puurunen, *J. Appl. Phys.*, 2005, **97**, 121301.
183 J. Guo, H. Van Bui, D. Valdesueiro, S. Yuan, B. Liang and J. R. Van Ommen, *Nanomaterials*, 2018, **8**, 61.
184 Z. Zhou, N. Zhou, X. Lu, M. ten Kate, D. Valdesueiro, J. R. van Ommen and H. T. (Bert) Hintzen, *RSC Adv.*, 2016, **6**, 76454–76462.
185 J. H. Woo, J. J. Travis, S. M. George and S.-H. Lee, *J. Electrochem. Soc.*, 2014, **162**, A344.
186 Y. Zhao, L. Yin, O. M. ten Kate, B. Dierre, R. Abellon, R.-J. Xie, J. R. van Ommen and H. T. Hintzen, *J. Mater. Chem. C*, 2019, **7**, 5772–5781.
187 M. Lee, W. Ahmad, D. W. Kim, K. M. Kwon, H. Y. Kwon, H.-B. Jang, S.-W. Noh, D.-H. Kim, S. J. A. Zaidi, H. Park, H. C. Lee, M. Abdul Basit and T. J. Park, *Chem. Mater.*, 2022, **34**, 3539–3587.
188 Z. Li, J. Su and X. Wang, *Carbon*, 2021, **179**, 299–326.
189 W.-J. Lee, S. Bera, H. Woo, H. G. Kim, J.-H. Baek, W. Hong, J.-Y. Park, S.-J. Oh and S.-H. Kwon, *Chem. Mater.*, 2022, **34**, 5949–5959.
190 M. Li, S. Saedy, S. Fu, T. Stellema, R. Kortlever and J. R. van Ommen, *Catal. Sci. Technol.*, 2024, **14**, 1328–1335.
191 J. Guo, D. Benz, T.-T. Doan Nguyen, P.-H. Nguyen, T.-L. Thi Le, H.-H. Nguyen, D. La Zara, B. Liang, H. T. (Bert) Hintzen, J. R. van Ommen and H. Van Bui, *Appl. Surf. Sci.*, 2020, **530**, 147244.
192 O. Muraza and A. Galadima, *Int. J. Energy Res.*, 2015, **39**, 1196–1216.
193 X. Gao, Z. Ge, G. Zhu, Z. Wang, J. Ashok and S. Kawi, *Catalysts*, 2021, **11**, 1003.
194 J. Lu, B. Fu, M. C. Kung, G. Xiao, J. W. Elam, H. H. Kung and P. C. Stair, *Science*, 2012, **335**, 1205–1208.
195 S. Min Kim, A. Armutlulu, W.-C. Liao, D. Hosseini, D. Stoian, Z. Chen, P. M. Abdala, C. Copéret and C. Müller, *Catal. Sci. Technol.*, 2021, **11**, 7563–7577.
196 X. Wang, B. Jin, Y. Jin, T. Wu, L. Ma and X. Liang, *ACS Appl. Nano Mater.*, 2020, **3**, 2867–2874.
197 R. Zhao, X. Du, K. Cao, M. Gong, Y. Li, J. Ai, R. Ye, R. Chen and B. Shan, *Int. J. Hydrogen Energy*, 2023, **48**, 28780–28791.
198 T. O. Kääriäinen, M. Kemell, M. Vehkamäki, M.-L. Kääriäinen, A. Correia, H. A. Santos, L. M. Bimbo, J. Hirvonen, P. Hoppu, S. M. George, D. C. Cameron, M. Ritala and M. Leskelä, *Int. J. Pharm.*, 2017, **525**, 160–174.
199 D. La Zara, F. Sun, F. Zhang, F. Franek, K. Balogh Sivars, J. Horndahl, S. Bates, M. Brännström, P. Ewing, M. J. Quayle, G. Petersson, S. Folestad and J. R. van Ommen, *ACS Nano*, 2021, **15**, 6684–6698.
200 D. E. Moseson, E. G. Benson, Z. Cao, S. Bhalla, F. Wang, M. Wang, K. Zheng, P. K. Narwankar, G. J. Simpson and L. S. Taylor, *Mol. Pharmaceutics*, 2023, **20**, 593–605.
201 V. P. Cao, K.-H. T. Dinh, P. H. Bui, Q. V. Hoang, T. H. Tran and H. V. Bui, *Appl. Surf. Sci.*, 2025, **687**, 162283.
202 D. Zhang, M. J. Quayle, G. Petersson, J. R. van Ommen and S. Folestad, *Nanoscale*, 2017, **9**, 11410–11417.
203 R. L. Garcea, N. M. Meinerz, M. Dong, H. Funke, S. Ghazvini and T. W. Randolph, *npj Vaccines*, 2020, **5**, 1–8.
204 A. E. Witeof, W. D. McClary, L. T. Rea, Q. Yang, M. M. Davis, H. H. Funke, C. E. Catalano and T. W. Randolph, *J. Pharm. Sci.*, 2022, **111**, 1354–1362.
205 A. E. Witeof, N. M. Meinerz, K. D. Walker, H. H. Funke, R. L. Garcea and T. W. Randolph, *J. Pharm. Sci.*, 2023, **112**, 2223–2229.
206 S. W. Brubaker, I. R. Walters, E. M. Hite, L. R. Antunez, E. L. Palm, H. H. Funke and B. L. Steadman, *Vaccines*, 2024, **12**, 761.

207 J. Hellrup, M. Rooth, A. Johansson and D. Mahlin, *Int. J. Pharm.*, 2017, **529**, 116–122.
208 C. Hirschberg, N. S. Jensen, J. Boetker, A. Ø. Madsen, T. O. Kääriäinen, M.-L. Kääriäinen, P. Hoppu, S. M. George, M. Murtomaa, C. C. Sun, J. Risbo and J. Rantanen, *Org. Process Res. Dev.*, 2019, **23**, 2362–2368.
209 D. L. Zara, F. Zhang, F. Sun, M. R. Bailey, M. J. Quayle, G. Petersson, S. Folestad and J. R. van Ommen, *Appl. Mater. Today*, 2021, **22**, 100945.
210 F. Zhang, K. Wu, D. La Zara, F. Sun, M. J. Quayle, G. Petersson, S. Folestad, J. W. Chew and J. R. van Ommen, *Chem. Eng. J.*, 2023, **462**, 142131.
211 S. Gupta, M. Mittal and A. S. Rathore, *ACS Appl. Mater. Interfaces*, 2022, **14**, 27195–27202.
212 S. Swaminathan, B. Ganapathy, M. Wang, F. Wang, J. Wooding, J. Frankel, S. Chiruvolu, S. Rengarajan and P. Narwankar, *Powder Technol.*, 2023, **425**, 118525.
213 L. S. Taylor and G. G. Z. Zhang, *Adv. Drug Delivery Rev.*, 2016, **101**, 122–142.
214 Y. Huang and W.-G. Dai, *Acta Pharm. Sin. B*, 2014, **4**, 18–25.
215 D. E. Moseson and L. S. Taylor, *Mol. Pharmaceutics*, 2023, **20**, 4802–4825.
216 D. E. Moseson, E. G. Benson, H. T. Nguyen, F. Wang, M. Wang, K. Zheng, P. K. Narwankar and L. S. Taylor, *ACS Appl. Mater. Interfaces*, 2022, **14**, 40698–40710.
217 T. Van Duong, H. T. Nguyen, F. Wang, M. Wang, P. K. Narwankar and L. S. Taylor, *Int. J. Pharm.*, 2022, **620**, 121747.
218 E. G. Benson, D. E. Moseson, S. Bhalla, F. Wang, M. Wang, K. Zheng, P. K. Narwankar and L. S. Taylor, *J. Pharm. Sci.*, 2025, **114**, 323–335.
219 D. Zhang, D. La Zara, M. J. Quayle, G. Petersson, J. R. van Ommen and S. Folestad, *ACS Appl. Bio Mater.*, 2019, **2**, 1518–1530.
220 J. Hellrup, M. Rooth, E. Mårtensson, K. Sigfridsson and A. Johansson, *Eur. J. Pharm. Biopharm.*, 2019, **140**, 60–66.
221 Indomethacin, https://go.drugbank.com/drugs/DB00328, accessed April 14, 2025.
222 Nanexa invites to a webcast to present the positive clinical data from NEX-22 once monthly GLP-1, liraglutide project published on last Friday, https://nanexa.com/en/mfn_news/nanexa-invites-to-a-webcast-to-present-the-positive-clinical-data-from-nex-22-once-monthly-glp-1-liraglutide-project-published-on-last-friday/, accessed April 14, 2025.
223 S. Stegemann, F. Leveiller, D. Franchi, H. de Jong and H. Lindén, *Eur. J. Pharm. Sci.*, 2007, **31**, 249–261.
224 Y. Liu, Y. Liang, J. Yuhong, P. Xin, J. L. Han, Y. Du, X. Yu, R. Zhu, M. Zhang, W. Chen and Y. Ma, *Drug Des., Dev. Ther.*, 2024, **18**, 1469–1495.
225 B. Ganapathy, V. Redasani, S. Debnath, N. Gupta, A. Kadam, F. Wang and P. Narwankar, *J. Pharm. Sci.*, 2025, **114**, 617–625.
226 D. Gunwal, B. Dutt, M. Choudhary and V. Budhwar, *Int. J. Res. Pharm. Sci.*, 2021, **12**, 2164–2172.
227 N. A. Vogel, P. S. Williams, A. H. Brozena, D. Sen, S. Atanasov, G. N. Parsons and S. A. Khan, *Adv. Mater. Interfaces*, 2015, **2**, 1500229.
228 G. Pilcer, N. Wauthoz and K. Amighi, *Adv. Drug Delivery Rev.*, 2012, **64**, 233–256.
229 S. Baghel, H. Cathcart and N. J. O'Reilly, *J. Pharm. Sci.*, 2016, **105**, 2527–2544.
230 L. A. Wegiel, L. J. Mauer, K. J. Edgar and L. S. Taylor, *J. Pharm. Sci.*, 2013, **102**, 171–184.
231 A. L. Onugwu, C. S. Nwagwu, O. S. Onugwu, A. C. Echezona, C. P. Agbo, S. A. Ihim, P. Emeh, P. O. Nnamani, A. A. Attama and V. V. Khutoryanskiy, *J. Controlled Release*, 2023, **354**, 465–488.
232 V. Phuong Cao, K.-H. Thi Dinh, T. Duc Dinh, P. Huu Bui, T. Hiep Tran and H. V. Bui, *Chem. Commun.*, 2025, **61**, 6186–6189.
233 M. A. A. Saikh, *J. Drug Delivery Ther.*, 2022, **12**, 126–138.
234 S. Just, G. Toschkoff, A. Funke, D. Djuric, G. Scharrer, J. Khinast, K. Knop and P. Kleinebudde, *Int. J. Pharm.*, 2013, **457**, 1–8.
235 H. Patil, R. V. Tiwari and M. A. Repka, *AAPS PharmSciTech*, 2016, **17**, 20–42.
236 L. K. Prasad, J. W. McGinity and R. O. Williams, *Int. J. Pharm.*, 2016, **505**, 289–302.
237 H. C. Guo, E. Ye, Z. Li, M.-Y. Han and X. J. Loh, *Mater. Sci. Eng., C*, 2017, **70**, 1182–1191.
238 O. Ireneusz, C. Marcin, S. Mateusz, L. Karolina, O. Marcin and P. Mateusz, *Adv. Sci. Technol. Res. J.*, 2021, **15**, 228–246.
239 S. Morooka, K. Kusakabe, A. Kobata and Y. Kato, *J. Chem. Eng. Jpn.*, 1988, **21**, 41–46.
240 M. Bartels, W. Lin, J. Nijenhuis, F. Kapteijn and J. R. van Ommen, *Prog. Energy Combust. Sci.*, 2008, **34**, 633–666.
241 T. Nozaki, X. Chen, D.-Y. Kim and H.-H. Kim, *Curr. Opin. Green Sustainable Chem.*, 2025, **51**, 100984.
242 Z. Wang, Z. Lei, R. Hong, M. Li and X. He, *Chem. Eng. J.*, 2025, **514**, 163086.
243 Y.-L. Wu, N. Putcha, K. W. Ng, D. T. Leong, C. T. Lim, S. C. J. Loo and X. Chen, *Acc. Chem. Res.*, 2013, **46**, 782–791.
244 N. Blal, G. Bardi, P. P. Pompa and D. Guarnieri, *Adv. Funct. Mater.*, 2024, **34**, 2408436.
245 Q. Yang, W. Yuan, X. Liu, Y. Zheng, Z. Cui, X. Yang, H. Pan and S. Wu, *Acta Biomater.*, 2017, **58**, 515–526.
246 L. Liu, R. Bhatia and T. J. Webster, *Int. J. Nanomed.*, 2017, **12**, 8711–8723.
247 D. S. Finch, T. Oreskovic, K. Ramadurai, C. F. Herrmann, S. M. George and R. L. Mahajan, *J. Biomed. Mater. Res., Part A*, 2008, **87A**, 100–106.
248 P. M. Piechulla, M. Chen, A. Goulas, R. L. Puurunen and J. R. van Ommen, *Chem. Mater.*, 2026, **38**, 20–86.